

## Diversity of eruptive styles inferred from the microlites of Mt Pelée andesite (Martinique, Lesser Antilles)

Caroline Martel<sup>a</sup> and Stéphane Poussineau<sup>a</sup>

<sup>a</sup>Institut des Sciences de la Terre d'Orléans, CNRS-INSU / Université d'Orléans (ISTO), Orléans, France

### Abstract

We have studied the compositional and textural characteristics of plagioclase microlites from several dome-forming eruptions (dome, block-and-ash flows, and surges) and plinian fallouts of the recent period of activity of Mt. Pelée in order to infer magma ascent dynamics. Dome-forming and plinian samples display a wide range of plagioclase microlite compositions, from An<sub>35</sub> to An<sub>90</sub> and An<sub>55</sub> to An<sub>90</sub>, respectively. Microlites with compositions > An<sub>50-60</sub>

crystallized from a mafic melt that intruded the andesitic reservoir in proportion of 10 vol.%. During magma ascent in the conduit, the fraction, number density, and morphology of the decompression-induced microlites (compositions < An<sub>50-60</sub>) suggest that the plinian magmas experienced a nucleation-dominated crystallization regime with high undercooling. In contrast magmas from domes and block-and-ash flows were dominated by a growth regime with low undercooling, and the surges were influenced by both regimes. According to these crystallization regimes and new experimental data on H<sub>2</sub>O content of the matrix glasses, we propose magma relative ascent rates and fragmentation pressures for the different eruptive styles observed at Mt. Pelée that may explain why surges are explosive events and why they may or may not be followed by a plinian event.

**Keywords:** microlites; H<sub>2</sub>O content; dome-forming eruptions; Plinian

### 1. Introduction

Many island-arc volcanic eruptions are characterized by dome-forming events that may produce pyroclastic flows and violent surges. The devastating 1902 May 8th surge at Mt. Pelée (Martinique) reminds us of the potentially high explosivity arising from growing domes. Dome-forming events may be directly followed or preceded by an explosive plinian event, but the transition between both eruptive styles still remains unpredictable and poorly understood. Because these eruptive regimes generate very different hazards, there is a crucial need to understand the factors responsible for either type of eruption, if we are to progress in the effort of evaluating hazards and forecasting island-arc silicic eruptions.

This complex eruptive behavior has been ascribed to different magma ascent rates within the volcanic conduit ([Jaupart and Allègre, 1991] and [Woods and Koyaguchi, 1994]) rather than pre-eruptive differences in volatile contents in the magma reservoir ([Barclay et al., 1996] and [Martel et al., 1998]). Low magma ascent rates permit bubble connectivity in the vesiculating magma and facilitate permeability developments with the surrounding rocks ([Klug and Cashman, 1996] and [Burgisser and Gardner, 2005]). This leads to a non-explosive open-

system degassing process, such as dome growth (Eichelberger et al., 1986). Conversely, high magma ascent rates prevent gas loss, leading to gas overpressure and a subsequent explosive closed-system degassing process, such as plinian events ([Villemant et al., 1996], [Sparks, 1997] and [Villemant and Boudon, 1998]). However, the ascent conditions that may lead to either explosive or effusive eruptions are not determined.

Upon ascent, gas exsolution from the melt induces an increase of the liquidus temperature of the silicate melt that may result in crystallization. The explosivity associated with high-velocity surges has been ascribed to large gas overpressures generated in highly viscous magmas at shallow depths in response to an extensive degassing-induced crystallization of microlites (Sparks, 1997). Therefore, preserved textures of microlites and degassing in the groundmass may provide valuable information on the magma decompression path and ascent rate, i.e. bubble and microlite sizes and number densities determined by nucleation and growth rates. Several studies have been devoted to the degassing-induced microlite crystallization in domes and block-and-ash flow deposits ([Cashman, 1992], [Cashman and Mangan, 1994], [Nakada et al., 1995], [Nakada and Motomura, 1999], [Hammer et al., 1999] and [Hammer et al., 2000]), but none exists on the microlite characteristics of explosive events (surges and plinian fallouts) or on the comparison between effusive and explosive eruptive styles. Recently, experimental studies have focused on the determination of magma ascent rates through timed decompressed experiments ([Geschwind and Rutherford, 1995], [Blundy and Cashman, 2001], [Hammer and Rutherford, 2002], [Martel and Schmidt, 2003], [Couch et al., 2003a], [Couch et al., 2003b] and [Larsen, 2005]), for which a prerequisite is a good knowledge of the natural products, the experimental charges should be compared with.

The specificity of each volcano in terms of eruptive behaviour, magma composition, and thermodynamic conditions makes necessary to investigate at first individual volcanic systems. We focus here on the recent eruptions of Mt. Pelée (Martinique, Lesser Antilles) for the following reasons: a) Mt. Pelée displays a large variety of eruptive styles from effusive to explosive events, b) the emplacement dynamics of the pyroclastic flows and surges have been carefully described ([Lacroix, 1904] and [Perret, 1935]), c) the deposit sequences are characterized in details ([Traineau et al., 1989a], [Bardintzeff et al., 1989], [Bourdier et al., 1989], [Charland and Lajoie, 1989], [Boudon and Lajoie, 1989], [Lajoie et al., 1989] and [Smith and Roobol, 1990]), and d) recent studies provide storage conditions for the andesitic and mafic magma reservoirs ([Fichaut et al., 1989], [Martel et al., 1998] and [Pichavant et al., 2002]) which constitute important statements for further investigation of the syn-eruptive thermodynamic conditions. In order to understand the eruption style variations observed at Mt. Pelée, we provide here a detailed study of the textural and compositional characteristics of the microlites and interstitial glasses for various eruptive events encompassing domes, pyroclastic flows, surges, and plinian fallouts that may contribute to the understanding of magma dynamics in island arc volcanism context.

## **2. Volcanological and petrological background**

### *2.1. Eruptive sequences*

The volcanic activity of Mt. Pelée is conveniently divided into three periods (Westercamp and Traineau, 1983). During the first stage (> 40 000 yr B.P.), an ancestral volcano formed of similar size and summit position to the present day (paleo-Pelée after Vincent et al., 1989). The second period (from 40 000 to 19 500 yr B.P.), also called the Saint Vincent stage, was dominated by pyroclastic ash-and-scoria flows of basaltic andesite composition (Vincent et

al., 1989). During the third stage or recent period (from 13 500 yr B.P. to present), the activity ranged between plinian and dome-forming eruptions of an andesitic magma. Dome-forming eruptions comprise phases of relatively quiescent lava-dome extrusions with associated destabilizations into more or less violent pyroclastic flows. Plinian eruptions are explosive events characterized by sustained columns of several kilometers high that may collapse into basal surges. In the well-documented 5000 yr B.P., the remains deposits of 6 plinian and 12 dome-forming eruptions have been identified ([Westercamp and Traineau, 1983] and [Smith and Roobol, 1990]).

The dome-forming eruptions of 1929–32 are the most recent volcanic activity of Mt. Pelée. These eruptions were witnessed and well documented by Perret (1935). The activity consisted of dome extrusion pulses of a relatively degassed andesite in the summit crater coupled with destabilizations into block-and-ash flows channelled in the Rivière Blanche valley (*nuées ardentes* of Merapi-type) leading to thick deposits (several meters high) of ash and blocks up to metric size (Bourdier et al., 1989). The activity ended with a more quiescent growth of lava spines and domes. The dome-forming eruptions of 1902, first reported by Lacroix (1904) thirty years before, similarly started with pulses of growing domes, the destabilizations of which produced the high-energy and high-velocity unchanneled surges from 1902 May 8th to August 30th (*nuées ardentes* of pelean-type). The deposits are up to 20 cm in thickness and characterized by ashes and dense to moderately vesiculated grey lithics up to 1–2 cm in diameter ([Bourdier et al., 1989] and [Boudon et al., 1994]). These surge events were followed by block-and-ask flows channeled in the Rivière Blanche valley from October 1902 to November 1903.

The P1 eruption in the stratigraphy nomenclature of Westercamp and Traineau (1983) is the last recorded plinian event (dated to  $650 \pm 20$  yr B.P.), preceded by the P2 ( $1670 \pm 40$  yr B.P.), P3 ( $2010 \pm 140$  yr B.P.), and P4 ( $2440 \pm 70$  yr B.P.) plinian events. These deposits suggest a widespread pumice fallout event ( $\sim 0.1 \text{ km}^3$  dense rock equivalent) followed by thick valley-filled pumice flows (Traineau et al., 1989a). The plinian products dominantly consist of juvenile white ashes and pumices with minor fractions of grey dense lithics and oxidized xenoliths. Based on a higher pumice percentage in the P3 fallout and more xenolithics in the pumice flow deposit, P3 appears to be of a slightly higher intensity than the P1 or P2 events (Bardintzeff et al., 1989). The P1, P3, and P4 pumice fall deposits overlay a thin (up to 20 cm) fine-grained deposit of grey ashes and dense lithics. The absence of erosional surface between the ash-and-lithics and the pumice deposits suggests a time interval less than few days. As these lithic deposits have very similar features with the 1902 May 8th deposit (granulometry and geographical extension), they were interpreted as comparable eruptive events (Boudon et al., 1994). Therefore, as Lacroix (1904) reported that the 1902 May 8th surge was initiated from a sub-surface level (the magma was seen at the surface the preceding days), the P1, P3, and P4 surges are likely to have been initiated at very shallow levels. The P1, P3, and P4 eruptions offer the rare opportunity to study the transition between the dome-forming (surge) and plinian eruptive style.

## *2.2. Magma compositions and pre-eruption conditions*

The recent activity of Mt. Pelée tapped a homogeneous andesitic magma ( $58 < \text{SiO}_2 < 65$  wt.%, 62 wt.% in average). The andesite is composed of 35 to 58 vol.% of phenocrysts (47 vol.% in average), encompassing 29–49 vol.% plagioclase, 4–9 vol.% orthopyroxene, 1–2 vol.% magnetite, minor ( $< 1$  vol.%) clinopyroxene, ilmenite and apatite, destabilized amphibole and olivine (both with reacted zones of

plagioclase + orthopyroxene + magnetite) ([Gourgaud et al., 1989] and [Martel et al., 1998]). These phenocrysts are embedded in a rhyolitic matrix glass (74–77 wt.% SiO<sub>2</sub>; Martel et al., 2000). The lack of variations in the physical and chemical conditions of magma storage preceding the recent eruptions stresses the bulk chemical homogeneity of the tapped andesitic magma body. The pre-eruptive storage conditions proposed for the andesitic part (62 wt.% SiO<sub>2</sub>) of the magma reservoir are 875–900 °C, 200 ± 50 MPa, an oxygen fugacity between NNO + 0.4 and + 0.8 and melt H<sub>2</sub>O contents of 5.3–6.3 wt.% (Martel et al., 1998). Yet, there is evidence for magma mixing in the 1902–1929 products recorded as mafic enclaves (51–59 wt.% SiO<sub>2</sub>) and few banded rocks ([Fichaut et al., 1989] and [Gourgaud et al., 1989]). Additionally, both plinian and dome-forming products contain a minor proportion of inherited phenocrysts, which originally grew from more mafic melt compositions ([Gourgaud et al., 1989] and [Pichavant et al., 2002]). Despite the lack of eruptions of mafic lavas in the recent period of activity (except as enclaves), we need to consider a broader context of a chemically-zoned magma chamber in the recent eruptive history, including a mafic reservoir (53 wt.% SiO<sub>2</sub>) at 950–1050 °C, 400 MPa, oxygen fugacity between NNO and NNO + 4 and a melt H<sub>2</sub>O contents around 6–8 wt.% (Pichavant et al., 2002). Therefore, it is extremely likely that both fractional crystallization and magma mixing are important in the petrogenesis of Mt. Pelée, but the respective role and proportion of these two processes remain undefined.

The products considered for our study are andesitic in bulk-rock composition with a rhyolitic matrix glass and come from various deposits that show unambiguous mechanisms of emplacement. These are dense lithics from the 1929 and 1902 domes, dense and vesiculated lithics from the 1929 block-and-ash flows (BAFs), the 1902 May 8th, 1902 August 30th, and P1 surges, and pumices from the P1, P2, P3, and P4 plinian fallouts (Table 1).

### 3. Methods

#### 3.1. Textural analyses

The samples chosen for the groundmass textural analyses (Table 1) belong to a much larger sampling of Mt. Pelée recent eruptions that was available for this study. For each eruptive sequence, we chose samples with representative microlite features (according to scanning electron microscopy (SEM) observations) and densities (according to the frequency histograms of the clast density/vesicularity in Martel et al., 2000). Thus, the surge samples of the 1902 May 8th were taken in the given mean porosity range, i.e., 31 ± 6 vol.%. The P1 surge displays a bimodal clast density distribution, so that we chose one sample in the mean mode (~ 30 vol.%) and a second in the low density part of the histogram. Both samples of the P1 plinian pumice are close to the mean porosity, but one is representative of the general pumice features, i.e., microlite-poor, whereas the second one represents rare microlite-rich pumices. The 1929 BAFs display the widest range of textural groundmasses (porosity from 5 to 65 vol.% and microlite-free to highly crystallized groundmasses; Martel et al., 2000). We chose samples with different porosity fractions and microlite contents representative of most of the observed samples. Such histograms are not available for the 1902 August 30th surge deposit and for the P2, P3, and P4 fallout deposits, but the chosen samples seem to be representative of the observed main characteristics.

Thin sections of the natural products were imaged by SEM, using a JEOL JSM-6400 (Polytech, Orléans). The crystal morphologies (symmetry axes and areas), areal fraction ( $\Phi$ ), and number density ( $N_A$ ) were determined by image analysis (Scion Image and SPO software; [Launeau and Robin, 1996] and [Launeau and Cruden, 1998]). We corrected stereologically

the two-dimensional (2D) parameters (major and minor axis) to provide true three-dimensional (3D) crystal habits using the spreadsheet program of Morgan and Jerram (2006). The database used in this program compares the sample's 2D measurements of minor-axis to major-axis ratios for non-foliated samples with standard 2D curves obtained from crystals of 703 different habits (ranging from 1:1:1–1:1:10–1:10:10 Short:Intermediate:Long axis). The output gives the five best-match standard curves and corresponding crystal habits based on a least-squares fit between sample and database. The authors suggest a minimum of ~200 crystal sections to robustly determine crystal habits if crystals are acicular in shape. The reliability of the shape is quoted as  $R^2$ , the fractional measure of the variation in the sample explained by the best-fit shape of the database ( $R^2$  values over 0.8 denote a good statistical fit, although care has to be taken when dealing with sample sets that involve less than about 200 crystal sections). Five of the eleven performed stereological conversions deal with less than 200 objects, with 3 of them having  $R^2$  values between 0.6 and 0.7. However, natural populations tend to display broader distributions than the idealised shapes of the database, mainly because they often exhibit non-unique shapes (Morgan and Jerram, 2006).

### 3.2. *Microlite and glass compositions*

Microlites and glasses were analysed using a Cameca SX 50 electron microprobe (BRGM-ISTO, Orléans) with a 6-nA beam current, a 15-kV accelerating voltage, 10-s counting time on peak, a focused beam for the crystals, focused and defocused beams of ~6  $\mu\text{m}$  in diameter for the glasses. The analytical errors on the oxide analyses are 1% relative for  $\text{SiO}_2$  and  $\text{Al}_2\text{O}_3$ , 2% for CaO, 3% for FeO, MgO, and  $\text{TiO}_2$ , and 5% for MnO,  $\text{Na}_2\text{O}$  and  $\text{K}_2\text{O}$ . Following the procedure of Pichavant (1987), alkali migration in glasses was corrected using hydrated rhyolitic glasses as standards with known alkali contents (determined by wet chemistry at the CRPG Nancy, France). Because the smallest population of the natural plagioclase microlites was below the effective beam size (~2  $\mu\text{m}$ ) of the electron microprobe, their chemical compositions had to be recalculated from analyses of plagioclase–glass mixtures. This assumes a known glass composition, analyzed with the same conditions as the crystals (focused beam, no correction for alkali loss, and no recalculation to 100 wt.%). However, when the total of the oxide analysis of the mixture was close to 100 wt.% (suggesting a dehydrated glass), the recalculation was performed with the glass recalculated to 100 wt.%. The recalculation procedure consisted of incrementally subtracting glass to the mixed composition until the resulting plagioclase composition (structural formula calculated on 8 oxygens) fulfilled the following conditions: total cations between 4.95 and 5.03, alkalis (Na + K + Ca) between 0.95 and 1.03, cations in the tetrahedral site (Si + Al) between 3.95 and 4.00, and an iron content (counted as FeO) below 1 wt.%. This recalculation sometimes provided slightly negative values (up to –0.10 wt.%) for  $\text{K}_2\text{O}$ , MgO, and  $\text{TiO}_2$ .

### 3.3. *Glass $\text{H}_2\text{O}$ contents*

The  $\text{H}_2\text{O}$  concentrations of natural glasses were determined by ion probe (Cameca IMS 3f, CRPG Nancy, France) following the procedure describe in Deloule et al. (1995). This analytical technique requires standard glasses with compositions close to the samples and known  $\text{H}_2\text{O}$  contents. Our hydrated standard glasses have the composition of the microlite-free interstitial glass of P1 fallout pumices (dry composition in wt.%: 76.33  $\text{SiO}_2$ , 0.29  $\text{TiO}_2$ , 13.33  $\text{Al}_2\text{O}_3$ , 2.24 FeO, 0.45 MgO, 2.93  $\text{Na}_2\text{O}$ , 2.43 CaO, 1.89  $\text{K}_2\text{O}$ ). The  $\text{H}_2\text{O}$  contents of the standards were determined by Karl–Fischer Titration (Mettler Toledo DL37) and Fourier Transform Infrared spectroscopy. The glasses from the P2 plinian fallout were determined by

the “by-difference” method using the electron microprobe, and calibrated for the glass H<sub>2</sub>O-dependence of the alkali loss (Devine et al., 1995).

In order to estimate the quenching/fragmentation pressures of our natural glasses using their H<sub>2</sub>O contents, we needed H<sub>2</sub>O solubility laws. Several reasons led us to get our own H<sub>2</sub>O solubility data: 1) H<sub>2</sub>O solubility models depend on glass composition (i.e., the alkali content; Burnham, 1979); 2) small uncertainties in the determination of the glass H<sub>2</sub>O contents lead to large variations in the saturation pressures at low pressures; 3) Data on H<sub>2</sub>O solubility are sporadic and scattered at pressures ≤ 50 MPa (Liu et al., 2005, and references herein). Therefore, we performed H<sub>2</sub>O solubility experiments at pressures ≤ 50 MPa starting with the interstitial glass composition of Mt. Pelée (same as the ion probe standards below). Bubble-

free glass pieces (~ 100 mg) were sealed into Au capsules with excess deionized H<sub>2</sub>O (10 wt.%) and loaded in an internally-heated pressure vessel (Basset Type, Ar pressure medium, Mo wires, isobaric quench) at 1040 °C and 51, 24 and 11 MPa for 170 h. Glass H<sub>2</sub>O contents were determined by Karl Fischer Titration: 2.23 (0.01), 1.13 (0.00), 0.98 (0.04) wt.% at 51, 24, and 11 MPa, respectively (average of three analyses with statistical error in bracket). The H<sub>2</sub>O solubility ( $C_{H_2O(P,T)}$ ) for our Mt. Pelée glass compositions at  $T$  (°C; empirically corrected using the model of Newman and Lowenstern, 2002) and  $P$  (MPa; ≤ 55 MPa) can be expressed as following:

$$C_{H_2O(P,T)} = \sqrt[1.6216]{\frac{P}{15.36}} + [2.79 \cdot 10^{-3} \times P + 8.66 \cdot 10^{-4} \times (1040 - T)]$$

The uncertainty is 10% for  $C_{H_2O}$  and ± 2 MPa for  $P$  corresponding to the manometer resolution at low pressures. At 50 MPa and 875 °C, Fig. 1 shows that the model of Burnham (1994) overestimates H<sub>2</sub>O solubility by 0.5 wt.%. However, this model is extrapolated for pressures < 50 MPa. The model of Liu et al. (2005) combines compiled experimental data from the literature with new experimental data at low pressures (0.1–25 MPa). Our data are slightly lower than those of Liu et al. (2005): a difference of 0.2 wt.% at 50 MPa and 0.1 wt.% at 10 MPa and 875 °C. Although, these solubility laws are close to the uncertainty of 15 and 10% given by Liu et al. (2005) and us, respectively, we will further use our solubility law for consistency with our natural products (comparable composition and analytical procedure).

#### 4. Results

The microlite paragenesis of the rhyolitic groundmass of Mt. Pelée andesite consists of plagioclase (> 95 vol.%), orthopyroxene (< 5 vol.%), Fe–Ti oxides (< 1 vol.%), and rare clinopyroxenes, as illustrated in Fig. 2. In this study, we will only consider plagioclase microlites, the other phases being not representative enough. We defined microlites on size and habit criteria. To a first approximation, we chose to consider a broad range of microlite sizes, with areas up to 3000 μm<sup>2</sup> and long axes up to 100 μm, as arbitrarily defined by Murphy et al. (2000). However, the morphological study concerns the microlite fraction with length below 20 μm, small and large microlites having different genetic origins, as explained later in the discussion. Some of the plagioclases with apparent sizes in the range defined

above were clearly pieces of broken crystals, as they were not crystal faceted or displayed abruptly interrupted chemical zonings. Broken crystals appear in nearly all eruptive deposits (particularly in P2 fallout), and were not included in our study.

#### 4.1. Microlite compositions

The dataset of 296 analyses of plagioclase microlites from various eruptive sequences of Mt. Pelée given in Martel et al. (2006) is supplemented here by 92 new analyses mainly concerning the smallest population size (1–5  $\mu\text{m}$ ), for which a procedure of composition recalculation was necessary (Table 2).

The plagioclase microlite compositions for the recent eruptions of Mt. Pelée are displayed along the ordinate axis of Fig. 3. The compositional range actually varies from a thin section to another within a particular eruptive sequence. These heterogeneities are not attributed to variations in the sample groundmass porosity (calculated by image analyses or from density measurements in Martel et al., 2000) and seem to reflect true compositional variations within a particular eruptive deposit. Plagioclase microlites in samples from dome-forming eruptions (domes, BAFs, and surges from the 1929, 1902, and P1 events) and microlite-rich pumices from the P1 and P4 plinian events show the largest compositional range from  $\text{An}_{30-40}$  to  $\text{An}_{80-90}$ . In contrast, microlite-poor (< 1 vol.%) pumices from the P1, P2, and P3 plinian events lack small plagioclases (1–5  $\mu\text{m}$ ) and plagioclase less calcic than the phenocryst rims, i.e. <  $\text{An}_{50-60}$  (with one exception in P1). The largest plagioclase microlites (> 20  $\mu\text{m}$  in length) often show visible zonings, the analytical profiles of which reveal a calcic-rich core ( $\text{An}_{80-90}$ ) surrounded by a sodic rim (<  $\text{An}_{60}$ ; Fig. 4). In the 10–20  $\mu\text{m}$  microlite size range, plagioclase cores only reach  $\text{An}_{65-70}$  (Fig. 4C–D). Below 10  $\mu\text{m}$  in length, most of the microlites lack visible chemical zonings, generally with compositions below the phenocryst rims (Fig. 5A–B), although some plinian pumices display small (5–10  $\mu\text{m}$ ) highly-calcic microlites (Fig. 5C).

#### 4.2. Areal fraction $\Phi$ , number density $N_A$ , and size of the plagioclase microlites

The plagioclase-microlite  $\Phi$  and  $N_A$ , both recalculated on a phenocryst-and bubble-free basis, and the corresponding mean size  $S_n (= (\Phi/N_A)^{0.5})$  are reported in Table 3. In dome products,  $\Phi$  and  $N_A$  are difficult to determine, first because the microlite outlines are barely distinguishable from the surrounding matrix (Fig. 2A), and second because of the precipitation of abundant amorphous silica. In fact, the 1929 BAFs and the 1902 surge deposits show two main textures of silica precipitations that we attribute to different mechanisms. The first texture is pervasive silica throughout the glass (Fig. 2B; middle of Fig. 2F) that we attribute to precipitations from the melt once  $\text{SiO}_2$  saturation is reached upon decompression and/or cooling (to quartz-feldspar cotectic; Blundy and Cashman, 2001). This hypothesis is mainly supported by phase equilibria experiments performed starting with a rhyolite melt at high temperatures (800–850 °C) and low pressures (< 125 MPa), in which a pervasive silica phase precipitates without any contribution of external fluid percolation ([Martel and Schmidt, 2003] and [Martel et al., 2006]). The second texture is described as spots of cracked silica located along the pores or with a recognizable pore shape (upper right and lower left corners of Fig. 2F) that could result from silica deposition during fluid percolation in the pore network. In this latter case, the estimation of  $\Phi$  and  $N_A$  (recalculated on a pore-free basis) should not take into account the silica volume that represents material addition. In contrast, silica precipitations from the melt may represent a real volume of this melt and thus may be counted as groundmass. In the dome

samples, there are large areas of cracked silica that may be ascribed to deposition from fluid percolation. However, the origin of the silica that resembles the pervasive type is difficult to attribute, because they largely touch pores (Fig. 2A). Moreover, a significant contribution of fluid percolation would not be surprising, given that the domes of Mt. Pelée are intensively percolated by hot fluids (Traineau et al., 1989b). Therefore, for the domes, we recalculated both  $\Phi$  and  $N_A$  for the supposed cases of silica-bearing and silica-free matrix glass, suspecting the true value is in between these two extreme cases.

Table 3 and Fig. 6 show that the 1902 and 1929 dome samples display  $\Phi$  between 0.30 and 0.60, depending on the origin of the silica phase. The 1902, August 30th and May 8th surges that preceded the 1902 dome have  $\Phi$  comparable to the lower value of the 1902 dome (recalculated on a silica precipitation-free basis), i.e., between 0.22–0.32. However, if fluid percolation is the dominant process for the silica phase deposition, then the 1902 surge groundmasses are half crystallized compared to the dome. The 1929 BAFs samples have rather small  $\Phi$ , up to 0.15. The P1 surge samples have comparable  $\Phi$  (0.22–0.28) to the 1902 surges. The common pumices from the plinian events are microlite-poor, with  $\Phi \leq 0.03$  (e.g., P1, P2, P3). However, some of the pumices of these plinian events contain more microlites, with  $\Phi$  up to 0.15 (e.g., P1, P4), referred here as to microlite-rich plinian pumices. Microlite  $N_A$  spans nearly 2.5 orders of magnitude. The domes and the 1929 BAFs have comparable  $N_A$ , around 15–40 and 6–27  $\times 10^3 \text{ mm}^{-2}$ , respectively. This compares to the 0–10  $\times 10^3 \text{ mm}^{-2}$   $N_A$  analyzed in the BAFs deposits of the 1989–1990 dome-collapse eruptions of the Redoubt volcano, Alaska (Wolf and Eichelberger, 1997). In contrast, the 1902 and P1 surges have  $N_A$  ten times higher than in the dome and BAFs products, i.e., 117–201 and 141–245  $\times 10^3 \text{ mm}^{-2}$ , respectively. The microlite-poor plinian pumices have  $N_A$  below 5  $\times 10^3 \text{ mm}^{-2}$ , whereas the microlite-rich pumices have  $N_A$  around 28–176  $\times 10^3 \text{ mm}^{-2}$ .

The measured areas of the plagioclase microlites are presented in Table 2 and shown along the abscissa axis of Fig. 3. It appears that microlites with compositions below  $\text{An}_{50-60}$  have restricted areas  $< 200 \mu\text{m}^2$ , whereas anorthite-richer crystals span the whole range between 10 to 3000  $\mu\text{m}^2$ . Microlite sizes may also be assessed through the mean sizes  $S_n = (\Phi/N_A)^{0.5}$

(Table 3 and Fig. 6). The microlites from the domes have large  $S_n$  of 4.5  $\mu\text{m}$ . The 1929 BAFs have lower  $S_n$ , around 2.4–2.9  $\mu\text{m}$ . The surge samples (1902 and P1) have comparable  $S_n$ , from 1.0 to 1.6  $\mu\text{m}$ . The high variability of the  $N_A$  in the plinian pumices, while relatively low  $\Phi$ , results in a large range of  $S_n$ , from 0.9 to 5.5  $\mu\text{m}$ .

#### 4.3. Shape of the plagioclase microlites

The crystal morphologies are linked to the temperature or the pressure ( $\text{H}_2\text{O}$  content) difference between the equilibrium phase liquidus and the effective nucleation and growth (Lofgren, 1974). Therefore, observations of the microlite shapes may provide information on their crystallization conditions. Fig. 7 shows the three main morphologies observed in the recent products of Mt. Pelée, i.e., tabular, skeletal, and dendritic. The tabular morphology (Fig. 7A), with rectangular to needle-like shapes depending on the planar crystal section, is essentially observed in the 1902 and 1929 domes and more rarely in the 1929 BAFs samples (Fig. 2A–B). Most of the 1929 BAFs, the 1902 and P1 surge samples have skeletal morphologies, including hopper and hourglass shapes, depending on the observed cross section (Faure et al., 2003; Fig. 2C, 5A). Few microlites in the surge samples and many of the microlite-rich plinian pumices show dendritic morphologies, including swallowtail

overgrowths on a hopper crystal and rod morphologies (Fig. 2E). The large microlites of the microlite-poor plinian pumices are tabular in shape, sometimes slightly rounded (Figs. 2D, 4F). In the 1929 BAFs and surge samples of 1902 and P1, the large zoned microlites are either purely tabular or tabular with skeletal overgrowths (Fig. 4A–B). In the microlite-rich pumices, these large microlites are mainly tabular with small dendritic overgrowths (Fig. 2 and Fig. 4E).

For a given sample, the microlite 2D aspect ratios analyzed in different images were gathered to be converted into 3D habits following the method of Morgan and Jerram (2006) (Table 3). Selected frequency histograms are shown in Fig. 8. The dome products, in which the proper outlines of the microlites could not be defined, and the microlite-poor pumices, for which the microlite number was not enough, were not considered. The results for the porous (porosity fraction of 0.44) 1929 BAFs suggest acicular 1.0:1.5:2.2 microlites (Fig. 8A), corroborated by the dense (porosity fraction of 0.15) sample (rectangular prisms of 1.0:1.5:1.8), although the 64 studied sections that lead to a low  $R^2$  value (0.59) are not enough to confirm the result. The 1902 August 30th, May 8th (Fig. 8B), and the P1 surge (Fig. 8D) samples display remarkable similar acicular microlite habit of 1.0:1.5–2.7:6.0–10.0, with reasonably confident estimations according to natural samples ( $R^2$  values between 0.67–0.81). The microlites in the P1 fallout pumices show rectangular-prism crystal habit of 1.0:3.0:7.0, with a good  $R^2$  value of 0.85 (Fig. 8C). In the P2 and P4 pumices, microlites are also rectangular prisms, but with different dimensions, i.e., 1.0:2.5:4.0 and 1.0:6.0:10.0, respectively. Despite the acceptable  $R^2$  values of 0.64 and 0.73 for P2 and P4 pumices, respectively, the very low number of analyzed sections (< 50) compels caution when considering these results.

#### *4.4. Composition, H<sub>2</sub>O content, and porosity of the groundmasses*

The glass compositions and their quartz-feldspar normative compositions are given in Table 4. In contrast to the glass data in Martel et al. (2000) that show an overall compositional range for a given eruptive deposit, the glasses have been analyzed here as close as possible to the microlites in order to trace the melt evolution with microlite crystallization. The matrix glasses are all rhyolitic, with SiO<sub>2</sub> contents ranging between 76 and 80 wt.%, and are around 73 wt.% for the P2 and P3 fallout eruptions.

The BAFs and surge samples show low mean H<sub>2</sub>O contents, from 0.17 to 0.84 wt.%, with maximum values of 1.31 wt.% (Table 5). The P1 and P2 plinian fallout deposits are H<sub>2</sub>O-rich, with  $1.8 \pm 0.3$  and  $2.5 \pm 0.3$  wt.%, respectively. The H<sub>2</sub>O data show a significant variability among several samples from a given eruptive unit, which seems to reflect true heterogeneities in the glass H<sub>2</sub>O contents.

The matrix porosities determined either by density measurements or by image analysis are shown in Table 3 and Table 5.

## 5. Discussion

### 5.1. Origin of the microlites and magma mixing process

Martel et al. (2006) identified two different origins for the plagioclase microlites in the recent eruptive products of Mt. Pelée, depending on their anorthite content. The plagioclase microlites with anorthite contents lower than the phenocryst rims (i.e.,  $An_{50-60}$ ) were considered to have crystallized from a water-saturated rhyolitic melt below 200 MPa during ascent towards the surface. This population is best represented in the dome-forming products (domes, BAFs, and surges) from the 1902 and 1929 eruptions, but almost lacks in the plinian eruptive products. The population with high anorthite contents ( $< An_{80}$ ) is ubiquitous in the recent deposits of Mt. Pelée. These crystals must have grown from andesitic to basaltic melts with water contents as high as 6–8 wt.%. Those melts most probably represent injections into the andesite body during episodes of recharge and mixing of the magma reservoir. The liquidus temperature of the basaltic andesite melt is 1050 °C at 400 MPa (Pichavant et al., 2002), so that the pressure and temperature contrast at the contact with the andesite ( $T = 875\text{--}900$  °C, 200 MPa; Martel et al., 1998) would generate up to 150 °C undercooling, appropriate for microlite crystallization. The chemical zonings observed in some of these high-Ca microlites (Fig. 4) suggests the possibility of either multi-stage growth or partial re-equilibration between early-formed crystals and the (rhyolitic) melt of the andesite at pre-eruptive conditions. If an eruption follows the mafic intrusion, further crystallization may occur in the conduit, giving rise to the population of microlite with compositions  $< An_{50-60}$  that may form either new crystals and/or rim the high-Ca microlites. This dual model of microlite genesis, i.e., basalt-inherited versus decompression-induced microlites, thus accounts for the whole compositional range of plagioclase microlites observed at Mt. Pelée.

The best way to distinguish between both microlite populations is certainly chemical composition (Martel et al., 2006). Yet, because analyzing each microlite from a particular section is a time-consuming task (specifically when crystals are below the spatial resolution of the electron microprobe beam), morphological information aiming at recognizing basalt-inherited from decompression-induced microlites may be helpful. The original shapes and sizes of the high-Ca basalt-inherited plagioclase microlites depend on their nucleation and growth conditions and on the time spent between the mafic magma intrusion and the reservoir exit. These original morphologies are potentially preserved in the plinian samples that lack further crystallization upon ascent to the surface. In these pumices, the highly-calcic plagioclase microlites have mean lengths varying from relatively small ( $< 10$  μm in the P2 pumices) to  $> 20$  μm, with tabular or slightly rounded shapes (Figs. 2D and 5C). If there was time for crystallization or re-equilibration during magma ascent, the original basalt-inherited microlites may be rimmed by low-Ca decompression-induced plagioclase, such as in the microlite-rich pumices or in dome-forming products (domes, BAFs and surges). In this case, microlites are characterized by oscillatory zonings that can be identified by backscattered electron microscopy, they are relatively large ( $> 20$  μm in length) and have tabular shapes (Fig. 4). In contrast, decompression-induced microlites lack visible chemical zonings, are small ( $< 10$  μm in length), and change shape from tabular to skeletal or dendritic with decreasing size. Some small zoned crystals (10–20 μm in length) present in the surge deposits (Fig. 4C–D) are difficult to classify into either basalt-inherited or decompression-induced microlites, because their cores have compositions of  $An_{65-70}$ , i.e., higher than the phenocryst rims, but not necessary requiring crystallization from a mafic melt (Martel et al., 2006).

Magma mixing is a well-identified process in the recent period of Mt. Pelée activity, notably through enclaves and banded rocks essentially in the early products of the 1902 (May 8th and 20th) and 1929 eruptions (Gourgaud et al., 1989). These textural features characterize volumetrically small mafic intrusions in comparison with the volume of the host silicic magma and a mechanical mixing process in which chemical equilibration is limited. When the proportion of involved mafic magma is small, the equilibration temperature is not much above the initial temperature of the host (Eichelberger et al., 2000). This may explain the absence of chemical and textural destabilizations of the phenocryst rims (such as reverse zonings and sieve-textures in plagioclases; [Gourgaud et al., 1989] and [Pichavant et al., 2002]) that are typical indicators of vigorous magma mixing processes ([Tsuchiyama, 1985] and [Browne et al., 2006]). In the products that lack textural traces of magma mingling events, such as the plinian fallouts, evidences of mixing are only provided by the basalt-inherited microlites.

Based on both natural and experimental data, Mt. Pelée magma storage region is viewed as a dynamic zoned reservoir, with a mafic magma intruding an andesitic upper reservoir ([Fichaut et al., 1989] and [Pichavant et al., 2002]). When the hot mafic magma (basaltic andesite, ~1050 °C, 6–8 wt.% H<sub>2</sub>O) intrudes the upper colder andesite (200 MPa, 875 °C, 6 ± 0.5 wt.%; Martel et al., 1998), it cools and crystallizes plagioclase microlites with compositions from An<sub>81–88</sub> to ~An<sub>60</sub>, driving the residual melt from basaltic andesite to rhyodacitic compositions (Martel et al., 2006).

An attempt to better constrain the proportion of the mafic magma involved in the mixing process has been realized through determinations of the number density ( $N_A$ ) and area fraction ( $\Phi$ , recalculated on a phenocryst-and bubble-free basis) of the basalt-inherited plagioclase microlites. These data are best estimated in the microlite-poor pumices in which no further decompression-induced crystallization occurred. The P1 and P3 plinian deposits have  $\Phi$  below 0.01 and  $N_A$  of maximum  $10^3 \text{ mm}^{-2}$ . The P2 plinian pumice has  $\Phi$  up to 0.04, with  $N_A$  of  $4 \times 10^3 \text{ mm}^{-2}$  (Table 3). In dome-forming products, the proportion of basalt-inherited microlites is much more difficult to assess, notably because of the late crystallizations around the original cores potentially causing re-equilibrations with time. Approximate measurements of Ca-rich cored microlites in the 1929 BAFs, 1902 May 8th and August 30th surges suggest  $\Phi$  and  $N_A$  below 0.21 and  $10^3 \text{ mm}^{-2}$ , respectively (Table 3). Although slightly underestimated, as a part of the crystallization took place around the pre-existing highly-calcic phenocrysts, this calculation suggests low proportions of magma mixing in Mt. Pelée reservoir during its recent period of activity, i.e., a mafic magma fraction of 0.01–0.10, maybe 0.20 for the 1902 August 30th surge. This is confirmed by the < 0.05 magma fraction estimated using the bulk composition data of the intruding magma (HAB in Pichavant et al., 2002), the pre-eruptive magma represented by the microlite-free P1 fallout (Martel et al., 1999) and the erupted products of the 1902 May 8th and August 30th surges and the 1929 BAFs (Gourgaud et al., 1989).

## **5.2. Ascent dynamics inferred from the decompression-induced microlites**

### *5.2.1. Crystallization regime*

During decompression, H<sub>2</sub>O exsolution from the melt raises the liquidus temperature of a water-rich magma. Thus, magma that was above or at the liquidus at high pressures becomes significantly undercooled during decompression, causing extensive groundmass crystallization. Microlite crystallization may be dominated by nucleation of new crystals or by growth around existing sites. Experimental studies have revealed that the nucleation-

dominated crystallization regime prevails at low pressures or for high decompression rates because of high undercoolings (supersaturations). In contrast, the growth-dominated crystallization regime is predominant at high pressures or for low decompression rates, for which undercooling is small ([Lofgren, 1980], [Kirkpatrick, 1981], [Hammer and Rutherford, 2002], [Couch et al., 2003a] and [Martel and Schmidt, 2003]). At extremely high undercoolings, the large driving force for crystallization is countered by limiting rates of diffusion and the melt may not crystallize.

In a diagram representing the microlite number density ( $N_A$ ) versus area fraction ( $\Phi$ ), samples for which the crystallization regime is nucleation-dominated over time would be characterized by a large  $N_A$  range with comparable  $\Phi$ , whereas a growth-dominated crystallization regime would show a large range of  $\Phi$  with comparable  $N_A$  (Hammer et al., 1999). In Fig. 6, the P1 fallout samples show similar  $\Phi$  (around 0.10) for  $N_A$  of nearly 2 orders of magnitude, leading to small mean sizes ( $S_n$ ) of  $\sim 1 \mu\text{m}$ . This suggests that the microlite crystallization regime in the plinian pumices is dominated by nucleation. In contrast, the 1929 BAFs samples show a horizontal trend with  $S_n$  values around 2.4–3.2  $\mu\text{m}$ , which suggests a crystallization regime dominated by growth on existing sites. The P1 and 1902 May 8th surge samples are overlapping, with  $S_n$  varying from 1 to 1.5  $\mu\text{m}$ . The crystallization in these latter samples is probably dominated by a combination between both regimes, as the data trend is rather vertical, but departs horizontally to higher  $\Phi$  (0.20–0.30) in comparison to the plinian trend. Based on time data for the different surge events at Mt. Pinatubo, the crystal size distribution (CSD) data of Hammer et al. (1999) indicate that supersaturation decreases with time, so that the style of crystallization switches from a nucleation-to a growth-dominated regime. Although we could not deduce any nucleation and growth rates from Mt. Pelée CSDs due to unknown crystallization durations, the comparison of the plots of the 1902 May 8th and succeeding August 30th in Fig. 6 and the presence of some tabular-shaped microlites in the August 30th deposit are consistent with a slight switch to a growth-dominated crystallization regime with time. We can note here that the sample porosity that results from gas loss and bubble collapse processes is not related to  $\Phi$  and  $N_A$ , as the two P1 surge samples with 0.29 and 0.68 pore fraction have comparable  $\Phi$  and  $N_A$  (Table 3). In other words, two samples from a given eruptive event may have crystallized under similar conditions resulting in similar microlite  $\Phi$  and  $N_A$ , while further experiencing different pore interconnectivity and permeability that finally lead to different sample porosities.

Experimental studies suggest a crystal shape evolution from tabular to skeletal and dendritic with the undercooling increase as the final pressure decreases ([Geschwind and Rutherford, 1995], [Blundy and Cashman, 2001], [Hammer and Rutherford, 2002], [Couch et al., 2003a] and [Martel and Schmidt, 2003]). This would agree with the variation in microlite morphology we found in Mt. Pelée samples: tabular morphologies are seen where  $N_A$  are small, i.e. for growth-dominated crystallization regime under small undercoolings, whereas dendritic shapes appear where  $N_A$  are high, in nucleation regimes under high undercoolings (Table 3).

### 5.2.2. Crystallization depth

The projection of the natural glasses into the synthetic system Qz–Ab–Or–H<sub>2</sub>O makes it possible to relate the evolution of the glass chemistry to decompression in sub-volcanic systems (Blundy and Cashman, 2001). The last glass composition may provide a means to infer the pressure (depth) of the last crystallization event at the time of magma quenching (fragmentation or cooling). The compositions of Mt. Pelée interstitial glasses have been

reported in Fig. 9. The glass compositions of the P1, 1902, and 1929 events follow a decompression-induced crystallization path, in which the plagioclase microlite fraction increases as the glass composition moves away from the albite component, up to the 50 MPa cotectic. An exception is the 0.13- $\Phi$  sample from the 1929 BAFs that comes from an eruption for which magma mixing has been identified to take place up to surface emplacement (Gourgaud et al., 1989), thus causing strong chemical disequilibria. Along the 50 MPa cotectic, the quartz saturation is reached and increasingly potassic feldspar crystallizes. On this projection, the most crystallized samples would suggest a quench level around 50 MPa. The P2 and P3 plinian pumices would suggest a quench event at H<sub>2</sub>O saturation pressure around 1000 MPa, which is not realistic. Several explanations can be proposed for these too high pressures. Firstly, we cannot assure P2 and P3 magmas have the same bulk-rock compositions and pre-eruptive conditions as the more recent eruptions. Secondly, the projection was originally designed for a QZ<sub>16</sub>Ab<sub>75</sub>Or<sub>9</sub> composition (Blundy and Cashman, 2001), whereas our glasses are QZ<sub>22-43</sub> and contain several other minor normative components (< 6 wt.%; diopside, hypersthene, ilmenite). This may potentially result in a significant shift of the cotectics. Thirdly, crystallization is a rather slow process, especially at low pressures for which kinetics are slow and may result in strong disequilibrium of the glass composition with pressure (experimentally observed at low pressures; Martel and Schmidt, 2003). In conclusion, fragmentation or quenching pressures deduced from major element melt compositions using the diagram of Blundy and Cashman (2001) do not provide precise enough information.

At low pressures, H<sub>2</sub>O contents of the interstitial glasses are better information to estimate fragmentation or quenching pressures than the glass composition data, because degassing and specifically H<sub>2</sub>O exsolution from melt is a fast process (Martel and Schmidt, 2003) that can rapidly reach equilibrium with decompression. The H<sub>2</sub>O content data suggest that the P1 fallout could have fragmented at 20–40 MPa and the P2 fallout at 40–70 MPa, considering a fragmentation temperature of 875 °C (pre-eruptive temperature; Table 5). This corresponds to fragmentation depths of around 1.5 and 2.5 km for P1 and P2, respectively. However, although degassing is a fast process, there is still the possibility that the extremely fast ascent of plinian magmas prevents degassing completion, resulting in an overestimation of the quenching depth. For dome-forming eruptions during which magma ascents are relatively slow, the H<sub>2</sub>O contents of the 1929 BAFs glasses suggest fragmentation or quenching pressures of 0–10 MPa, that is at depth below 450 m. The 1902 surges could have fragmented at pressure of 1–6 and 1–8 MPa for the May 8th and August 30th, respectively, that is between 50 and 400 m depth (Table 5). The heterogeneities in the H<sub>2</sub>O contents of different samples from a given eruption may either represent variability in quenching depths or local degassing disequilibrium.

### 5.2.3. Ascent rates

Following the conclusions of Geschwind and Rutherford (1995) and Wolf and Eichelberger (1997), we think that the observed differences in the groundmass characteristics may be caused by differing rates of magma ascent and crystallization dynamics. The absence of decompression-induced microlites in most of the plinian pumices (Fig. 3) suggests an ascent rate that is too fast for magma crystallization. The delay for plagioclase nucleation has been experimentally determined between 1 and 5 h ([Couch et al., 2003a] and [Larsen, 2005]) suggesting that ascent of the plinian magma from the reservoir must have been completed within 5 h. This is in agreement with the P1 eruption duration of 1–3 h proposed by Bardintzeff et al. (1989) based on grain-size and tephra volume considerations. The presence

of a silica phase may also provide information on magma residence time and depth. The 1902 and 1929 eruptions, i.e. domes, BAFs and surges, contain a silica phase that was analyzed as cristobalite by Raman spectroscopy (Martel et al., 2000). A silica phase is also present in the phase equilibrium experiments starting with the rhyolite melt at 850 °C and pressures < 75 MPa (Martel et al., 2006). These experiment durations of 1 week suggest that the domes, 1929 BAFs, and 1902 surges spent at least few days at pressures below 75 MPa. In contrast, the P1 surge samples do not contain any precipitated silica, which would either suggest a fragmentation pressure above 75 MPa or an insufficient residence time at pressure < 75 MPa for silica to precipitate. The former hypothesis can be ruled out by the data published in Martel et al. (2000) that suggest 1.8 wt.% maximum H<sub>2</sub>O in the glasses from P1 surge samples, corresponding to a maximum saturation pressure of 32 MPa. It is more likely that the residence time of P1 magma at low pressures was too short for silica precipitation.

#### 5.2.4. Eruption schemes

There could be a link between the small and constant volume proportions of mafic magma intrusions (< 10 vol.%) deduced from the basalt-inherited microlite fractions and the small and constant volumes of the recent emitted products at Mt. Pelée (~0.1 km<sup>3</sup>, dense-rock equivalent). If we assume the mafic intrusions triggered the eruptions, the groundmass modifications produced by the mafic magma mingling provide information on ascent dynamics.

In a general manner, the plinian magmas ascend within 1–5 h, which prevents any microlite crystallization before fragmentation at ~ 30–50 MPa. However, some parts of these plinian magmas, maybe along conduit borders, must have slowed down, permitting groundmass crystallization under a nucleated-dominated regime resulting in very small ( $S_n < 1 \mu\text{m}$ ) dendritic microlites. One of these microlites (An<sub>41</sub>, Fig. 3) corresponds to the equilibrium composition at 50 MPa or less (875 °C; Martel et al., 2006), in agreement with the fragmentation pressure inferred from glass H<sub>2</sub>O contents. The magmas from the domes and the BAFs ascend more slowly than the plinian magmas, as revealed by the characteristics of their decompression-induced microlites, i.e., large, mostly tabular or skeletal in shape, with continuum compositions from An<sub>50</sub> to An<sub>35</sub>, and a growth-dominated crystallization regime under small undercoolings (slow decompression rates and crystallization at shallow depth). This agrees with the conclusion of Nakada and Motomura (1999) that lower groundmass crystallinity correlates to higher effusion rates, which may be explained by the sluggish crystallization kinetics at low pressures. The An<sub>35</sub> microlites correspond to an equilibrium crystallization pressure of 10 MPa at 875 °C (Martel et al., 2006), which compares well with the pressures of 0–10 MPa deduced from the glass H<sub>2</sub>O contents (Table 5). The 1929 and 1902 BAFs were followed by dome growths, in which the magma continues to crystallize and silica precipitates from the melt and/or precipitates from fluid percolations. The surface level of crystallization and degassing and the absence of volume constraints (conduit walls) and lithostatic pressure reduce the possibility of dome explosions. The surge magmas must have spent more time at shallow depth than the BAFs, because they crystallized acicular microlites in a nucleation-dominantly crystallization regime (although contribution of a growth regime), that is, at higher pressures or with slower decompression rates than in the BAFs case. This massive groundmass crystallization at shallow level drastically increases the magma viscosity that contributes to generate excess pressures following the self-sealing plug model (Sparks, 1997). The sudden release of this pressure must lead to a violent explosion, as for the surges in 1902 and supposedly P1, P3, and P4. However, the P1 surge samples contain anorthite-rich microlites (An<sub>80–90</sub>) and no silica precipitations. This could suggest a faster ascent rate of the

magma before fragmentation than for the 1902 surges, because there was no time for the small basalt-inherited microlites to re-equilibrate at more albitic compositions and for the silica to precipitate at low pressures. It is interesting to note that the P1 surge was followed by a plinian fallout, in contrast to the 1902 surges. A possible hypothesis for the occurrence of the plinian event is that in comparison to the 1902 surges, the proposed higher ascent rate of the P1 magma prior to the surge event possibly prevented significant volatile loss in the surrounding rocks. A further rapid decompression of these trapped volatiles could be particularly violent and capable of triggering a sustained plinian event. In contrast, it is possible that in 1902, the magma ascended more slowly, maybe also closer to the surface, so that the magma column following the surge events had time to degas and finally extruded as a dome.

The next step of the study would concern the precise determination of the ascent rates for the plinian and dome-forming magmas through timed decompression experiments aiming at reproducing the degassing and crystallization processes upon ascent (microlite morphologies and compositions, final porosities and H<sub>2</sub>O contents), with the objective of better understand and predict the eruptive style of island-arc volcanism.

## Acknowledgments

We greatly thank A. Genty for the scanning electron microscope images, O. Rouer for help with the electron microprobe, E. Deloule and M. Champenois for the ion probe analyzes, and R. Champallier for help with the experimental device. We also thank F. Costa and M. J. Rutherford for constructive reviews of the manuscript. The study was funded by two French national research programs on the Antilles volcanism: ACI Antilles (T. Druitt) and ANR EXPLANT (C. Martel).

## References

- Barclay et al., 1996 J. Barclay, M.R. Carroll, B.F. Houghton and C.J.N. Wilson, Pre-eruptive volatile content and degassing history of an evolving peralkaline volcano, *Journal of Volcanology and Geothermal Research* **74** (1996), pp. 75–87.
- Bardintzeff et al., 1989 J.M. Bardintzeff, J.C. Miskovsky, H. Traineau and D. Westercamp, The recent pumice eruptions of Mt. Pelée volcano, Martinique. Part II: grain-size studies and modelling of the last plinian phase P1, *Journal of Volcanology and Geothermal Research* **38** (1989), pp. 35–48 Mount Pelée Special Issue.
- Blundy and Cashman, 2001 J. Blundy and K.V. Cashman, Ascent-driven crystallisation of dacite magmas at Mount St. Helens, 1980–1986, *Contributions to Mineralogy and Petrology* **140** (2001), pp. 631–650.
- Boudon and Lajoie, 1989 G. Boudon and J. Lajoie, The 1902 pelean deposits in the Fort Cemetery of St. Pierre, Martinique: a mode for the accumulation of turbulent nuées ardentes, *Journal of Volcanology and Geothermal Research* **38** (1989), pp. 113–130 Mount Pelée Special Issue.

Boudon et al., 1994 G. Boudon, J.-L. Bourdier and H. Traineau, High-energy pyroclastic flows in the recent activity of Mt. Pelée, Martinique, *IAVCEI Abstracts, International Volcanological Congress, Ankara, Turkey* (1994).

Bourdier et al., 1989 J.-L. Bourdier, G. Boudon and A. Gourgaud, Stratigraphy of the 1902 and 1929 nuée-ardente deposits, Mt. Pelée, Martinique, *Journal of Volcanology and Geothermal Research* **38** (1989), pp. 77–96 Mount Pelée Special Issue.

Browne et al., 2006 B.L. Browne, J.C. Eichelberger, L.C. Patino, T.A. Vogel, K. Uto and H. Hoshizumi, Magma mingling as indicated by texture and Sr/Ba ratios of plagioclase phenocrysts from Unzen volcano, SW Japan, *Journal of Volcanology and Geothermal Research* **154** (2006), pp. 103–116.

Burgisser and Gardner, 2005 A. Burgisser and J.E. Gardner, Experimental constraints on degassing and permeability in volcanic conduit flow, *Bulletin of Volcanology* **67** (2005), pp. 42–56.

Burnham, 1979 C.W. Burnham, The importance of volatiles constituents. In: H.S. Yoder, Editor, *The Evolution of Igneous Rocks*, Princeton University press, Princeton, N.J (1979), pp. 439–482.

Burnham, 1994 C.W. Burnham, Development of the Burnham model for prediction of H<sub>2</sub>O solubility in magmas. In: M.R. Carroll and J.R. Holloway, Editors, *Volatiles in Magmas. Reviews in Mineralogical Society, American Mineralogy* vol. **30** (1994), pp. 123–129.

Cashman, 1992 K.V. Cashman, Groundmass crystallization of Mount St. Helens dacite 1980–1986: a tool for interpreting shallow magmatic processes, *Contributions to Mineralogy and Petrology* **109** (1992), pp. 431–449.

Cashman and Mangan, 1994 K.V. Cashman and M.T. Mangan, Physical aspects of magmatic degassing II. Constraints on vesiculation processes from textural studies of eruptive products. In: M.R. Carroll and J.R. Holloway, Editors, *Volatiles in Magmas. Reviews in Mineralogical Society, American Mineralogy* vol. **30** (1994), pp. 446–478.

Charland and Lajoie, 1989 A. Charland and J. Lajoie, Characteristics of pyroclastic deposits at the margin of Fond Canonville, Martinique, and implications for the transport of the nuées ardentes of Mt. Pelée, *Journal of Volcanology and Geothermal Research* **38** (1989), pp. 97–112 Mount Pelée Special Issue.

Couch et al., 2003a S. Couch, R.S.J. Sparks and M.R. Carroll, The kinetics of degassing-induced crystallization at Soufrière Hills volcano, Montserrat, *Journal of Petrology* **44** (2003), pp. 1477–1502.

Couch et al., 2003b S. Couch, C.L. Harford, R.S.J. Sparks and M.R. Carroll, Experimental constraints on the conditions of formation of highly calcic plagioclase microlites at Soufrière Hills volcano, Montserrat, *Journal of Petrology* **44** (2003), pp. 1455–1475

Deloule et al., 1995 E. Deloule, O. Paillat, M. Pichavant and B. Scaillet, Ion microprobe determination of water in silicate glasses: methods and applications, *Chemical Geology* **125** (1995), pp. 19–28.

Devine et al., 1995 J.D. Devine, J.E. Gardner, H.P. Brack, G.D. Layne and M.J. Rutherford, Comparison of microanalytical methods for estimating H<sub>2</sub>O contents of silicic volcanic glasses, *American Mineralogist* **80** (1995), pp. 319–328.

Eichelberger et al., 1986 J.C. Eichelberger, C.R. Carrigan, H.R. Westrich and R.H. Price, Non-explosive silicic volcanism, *Nature* **323** (1986), pp. 598–602.

Eichelberger et al., 2000 J.C. Eichelberger, D.G. Chertkoff, S.T. Dreher and C.J. Nye, Magmas in collision: rethinking chemical zonation in silicic magmas, *Geology* **28** (2000), pp. 603–606.

Faure et al., 2003 F. Faure, G. Trolliard, C. Nicollet and J.-M. Montel, A developmental model of olivine morphology as a function of the cooling rate and the degree of undercooling, *Contributions to Mineralogy and Petrology* **145** (2003), pp. 251–263.

Fichaut et al., 1989 M. Fichaut, R.C. Maury, H. Traineau, D. Westercamp, J.-L. Joron, A. Gourgaud and C. Coulon, Magmatology of Mt. Pelée (Martinique, F.W.I). III: Fractional crystallisation versus magma mixing, *Journal of Volcanology and Geothermal Research* **38** (1989), pp. 189–213 Mount Pelée Special Issue.

Geschwind and Rutherford, 1995 C.H. Geschwind and M.J. Rutherford, Crystallization of microlites during magma ascent: the fluid mechanics of 1980–1986 eruptions of Mt. St. Helens, *Bulletin of Volcanology* **57** (1995), pp. 356–370.

Gourgaud et al., 1989 A. Gourgaud, M. Fichaut and J.-L. Joron, Magmatology of Mt. Pelée (Martinique, F.W.I). I: Magma mixing and triggering of the 1902 and 1929 Pelean nuées ardentes, *Journal of Volcanology and Geothermal Research* **38** (1989), pp. 143–169 Mount Pelée Special Issue.

Hammer and Rutherford, 2002 J.E. Hammer and M.J. Rutherford, An experimental study of the kinetics of decompression-induced crystallization in silicic melts, *Journal of Geophysical Research* **107** (2002), pp. 1–23 ECV8.

Hammer et al., 1999 J.E. Hammer, K.V. Cashman, R.P. Hoblitt and S. Newman, Degassing and microlite crystallization during pre-climactic events of the 1991 eruption of Mt Pinatubo, Philippines, *Bulletin of Volcanology* **60** (1999), pp. 355–380.

Hammer et al., 2000 J.E. Hammer, K.V. Cashman and B. Voight, Magmatic processes revealed by textural and compositional trends in Merapi dome lavas, *Journal of Volcanology and Geothermal Research* **100** (2000), pp. 165–192

Jaupart and Allègre, 1991 C. Jaupart and C.J. Allègre, Gas content, eruption rate and instabilities of eruption regime in silicic volcanoes, *Earth and Planetary Science Letters* **102** (1991), pp. 413–429.

Kirkpatrick, 1981 R.J. Kirkpatrick, Kinetics of crystallization of igneous rocks. In: A. Lasaga and R.J. Kirkpatrick, Editors, *Kinetics of geochemical processes*, Mineralogical Society of America, Washington DC (1981), pp. 321–397.

Klug and Cashman, 1996 C. Klug and K.V. Cashman, Permeability development in vesiculating magmas: implications for fragmentation, *Bulletin of Volcanology* **58** (1996), pp. 87–100

Lacroix, 1904 A. Lacroix, La Montagne Pelée et ses éruptions, *Masson Paris* (1904) 662 p..

Lajoie et al., 1989 J. Lajoie, G. Boudon and J.-L. Bourdier, Depositional mechanics of the 1902 pyroclastic nuée-ardente deposits of Mt. Pelée, Martinique, *Journal of Volcanology and Geothermal Research* **38** (1989), pp. 131–142 Mount Pelée Special Issue.

Larsen, 2005 J.F. Larsen, Experimental study of plagioclase rim growth around anorthite seed crystals in rhyodacitic melt, *American Mineralogist* **90** (2005), pp. 417–427.

Launeau and Cruden, 1998 P. Launeau and A.R. Cruden, Magmatic fabric acquisition mechanisms in a syenite: results of a combined anisotropy of magnetic susceptibility and image analysis study, *Journal of Geophysical Research* **103** (1998), pp. 5067–5089.

Launeau and Robin, 1996 P. Launeau and P.Y. Robin, Fabric analysis using the intercept method, *Tectonophysics* **267** (1996), pp. 91–119.

Liu et al., 2005 Y. Liu, Y. Zhang and H. Behrens, Solubility of H<sub>2</sub>O in rhyolitic melts at low pressures and a new empirical model for mixed H<sub>2</sub>O–CO<sub>2</sub> solubility in rhyolitic melts, *Journal of Volcanology and Geothermal Research* **143** (2005), pp. 219–235.

Lofgren, 1974 G. Lofgren, An experimental study of plagioclase crystal morphology: isothermal crystallization, *American Journal of Science* **274** (1974), pp. 243–273.

Lofgren, 1980 G. Lofgren, Experimental studies on the dynamic crystallization of silicate melts. In: R.B. Hargraves, Editor, *Physics of magmatic processes*, Princeton University Press, New York (1980), pp. 487–565.

Martel and Schmidt, 2003 C. Martel and B.C. Schmidt, Decompression experiments as an insight into ascent rates of silicic magmas, *Contributions to Mineralogy and Petrology* **144** (2003), pp. 397–415.

Martel et al., 1998 C. Martel, M. Pichavant, J.-L. Bourdier, H. Traineau, F. Holtz and B. Scaillet, Magma storage conditions and control of eruption regime in silicic volcanoes: experimental evidence from Mt. Pelée, *Earth and Planetary Science Letters* **156** (1998), pp. 89–99.

Martel et al., 1999 C. Martel, M. Pichavant, F. Holtz, B. Scaillet, J.-L. Bourdier and H. Traineau, Effect of fO<sub>2</sub> and H<sub>2</sub>O on andesite phase relations between 2 and 4 kbars, *Journal of Geophysical Research* **104** (1999), pp. 29453–29470.

Martel et al., 2000 C. Martel, J.-L. Bourdier, M. Pichavant and H. Traineau, Textures, water content and degassing of silicic andesites from recent plinian and dome-forming eruptions at Mount Pelee volcano (Martinique, Lesser Antilles arc), *Journal of Volcanology and Geothermal Research* **96** (2000), pp. 191–206.

Martel et al., 2006 C. Martel, A. Radadi Ali, S. Poussineau, A. Gourgaud and M. Pichavant, Basalt-inherited microlites in silicic magmas: evidence from Mt. Pelée (Martinique, F.W.I.), *Geology* **34** (2006), pp. 905–908.

Morgan and Jerram, 2006 D.J. Morgan and D.A. Jerram, On estimating crystal shape for crystal size distribution analysis, *Journal of Volcanology and Geothermal Research* **154** (2006), pp. 1–7.

Murphy et al., 2000 M.D. Murphy, R.S.J. Sparks, J. Barclay, M.R. Carroll and T.S. Brewer, Remobilization of andesite magma by intrusion of mafic magma at Soufrière Hills volcano, Montserrat, West Indies, *Journal of Petrology* **41** (2000), pp. 21–42.

Nakada and Motomura, 1999 S. Nakada and Y. Motomura, Petrology of the 1990–1995 eruption at Unzen: effusion pulsation and groundmass crystallization, *Journal of Volcanology and Geothermal Research* **89** (1999), pp. 173–196 Unzen volcano Special issue.

Nakada et al., 1995 S. Nakada, Y. Motomura and H. Shimizu, Manner of magma ascent at Unzen Volcano (Japan), *Geophysical Research Letters* **22** (5) (1995), pp. 567–570.

Newman and Lowenstern, 2002 S. Newman and J.B. Lowenstern, VOLATILECALC: a silicate melt-H<sub>2</sub>O–CO<sub>2</sub> solution model written in Visual Basic for excel, *Computers & Geosciences* **28** (2002), pp. 597–604.

Perret, 1935 F.A. Perret, *The eruptions of Mt. Pelée 1929–1932* vol. **458**, Carnegie Institute Publications, Washington (1935) 126 p..

Pichavant, 1987 M. Pichavant, The effects of boron and water on liquidus phase relations in the haplogranite at 1 kbar, *American Mineralogist* **72** (1987), pp. 1056–1070.

Pichavant et al., 2002 M. Pichavant, C. Martel, J.-L. Bourdier and B. Scaillet, Physical conditions, structure, and dynamics of a zoned magma chamber: Mount Pelée (Martinique, Lesser Antilles Arc), *Journal of Geophysical Research* **107** (2002) 10.1029.

Smith and Roobol, 1990 A.L. Smith and M.J. Roobol, Mount Pelée, Martinique, A study of an active island-arc volcano, *Memoir - Geological Society of America* **175**. (1990) 105 p.

Sparks, 1997 R.S.J. Sparks, Causes and consequences of pressurisation in lava dome eruptions, *Earth and Planetary Science Letters* **150** (1997), pp. 177–189.

Traineau et al., 1989a H. Traineau, D. Westercamp, J.M. Bardintzeff and J.C. Mikovsky, The recent pumice eruptions of Mt. Pelée volcano, Martinique. Part I: Depositional sequences, description of pumiceous deposits, *Journal of Volcanology and Geothermal Research* **38** (1989), pp. 17–33 Mount Pelée Special Issue.

Traineau et al., 1989b H. Traineau, D. Westercamp and Y. Benderitter, Case study of a volcanic geothermal system, Mount Pelée, Martinique, *Journal of Volcanology and Geothermal Research* **38** (1989), pp. 17–33 Mount Pelée Special Issue.

Tsuchiyama, 1985 A. Tsuchiyama, Dissolution kinetics of plagioclase in the melt of the system diopside–albite–anorthite, and the origin of dusty plagioclase in andesites, *Contributions to Mineralogy and Petrology* **89** (1985), pp. 1–16.

Villemant and Boudon, 1998 B. Villemant and G. Boudon, Transition from dome-forming to plinian eruptive styles controlled by H<sub>2</sub>O and Cl degassing, *Nature* **392** (1998), pp. 65–69.

Villemant et al., 1996 B. Villemant, G. Boudon and J.-C. Komorowski, U-series disequilibrium in arc magmas induced by water–magma interaction, *Earth and Planetary Science Letters* **140** (1996), pp. 259–267.

Vincent et al., 1989 P.M. Vincent, J.-L. Bourdier and G. Boudon, The primitive volcano of Mount Pelée: its construction and partial destruction by flank collapse, *Journal of Volcanology and Geothermal Research* **38** (1989), pp. 1–16 Mount Pelée Special Issue.

Westercamp and Traineau, 1983 D. Westercamp and H. Traineau, The past 5000 years of volcanic activity at Mt. Pelée, Martinique (F.W.I.): Implications for assesement of volcanic hazards, *Journal of Volcanology and Geothermal Research* **17** (1983), pp. 159–185.

Wolf and Eichelberger, 1997 K.J. Wolf and J.C. Eichelberger, Syn-eruptive mixing, degassing, and crystallization at Redoubt Volcano, eruption of December, 1989 to May 1990, *Journal of Volcanology and Geothermal Research* **75** (1997), pp. 19–37

Woods and Koyaguchi, 1994 A.W. Woods and T. Koyaguchi, Transitions between explosive and effusive eruptions of silicic magmas, *Nature* **370** (1994), pp. 641–644.

## Figures

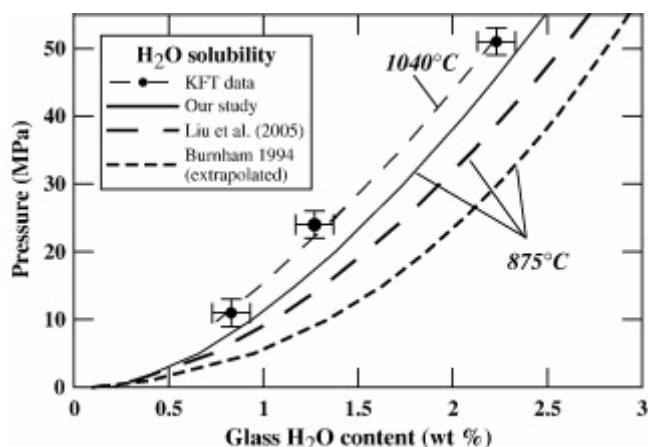


Fig. 1. H<sub>2</sub>O solubilities obtained at  $P \leq 55$  MPa starting from the rhyolitic crystal-free interstitial glass of P1 fallout pumices. The dots are the average of three Karl Fischer titration (KFT) measurements obtained on our glasses hydrated at 1040 °C. The fit of these data is the deduced solubility law at 1040 °C. The solid line represents our solubility law empirically corrected at 875 °C using the model of Newman and Lowenstern (2002) (see equation in text). Comparison is presented with the H<sub>2</sub>O solubility model of Burnham (1994) extrapolated at pressures < 50 MPa and Liu et al. (2005) given with relative uncertainties of 15%.

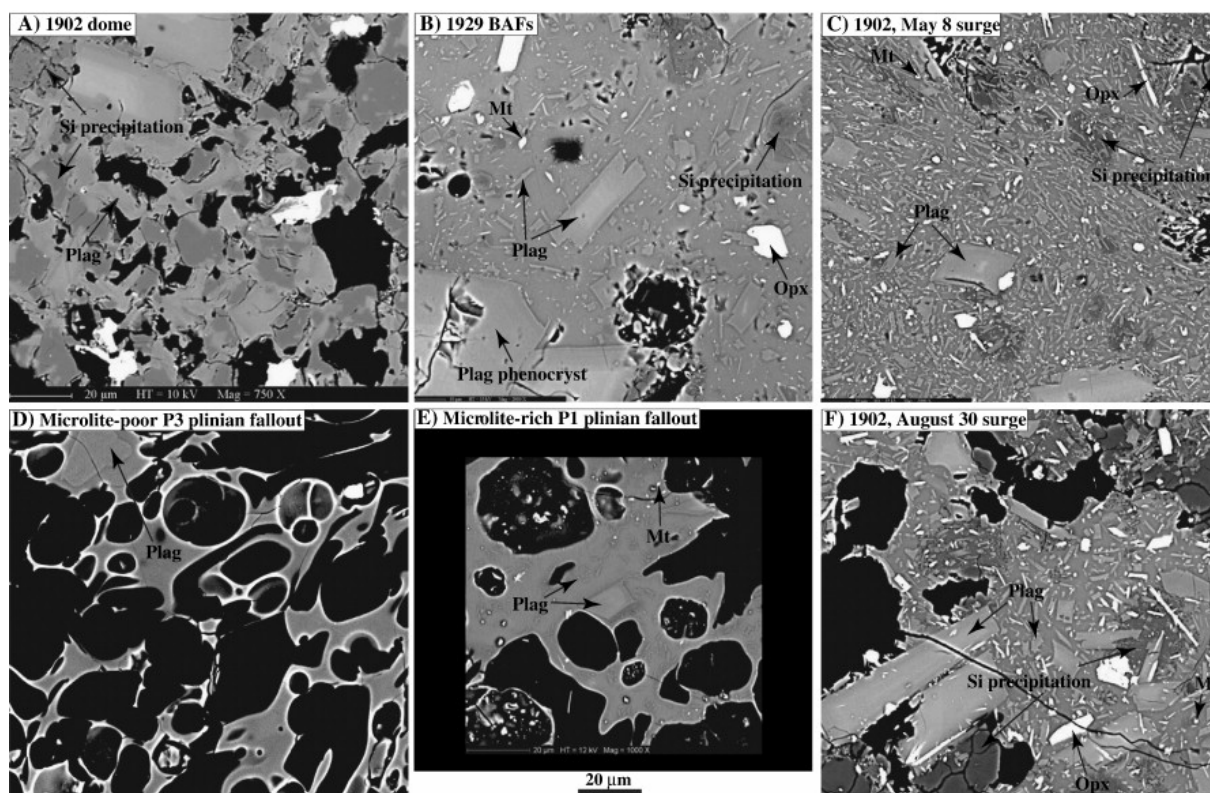


Fig. 2. SEM images showing the microlite textural characteristics in recent eruptive products of Mt. Pelée. A) MT34M, B) MT37N1, C) MT37B23, D) MT35G1, E) MT25E1, and F) MT36V15 (see Table 1). Scale bar of 20 µm for all images

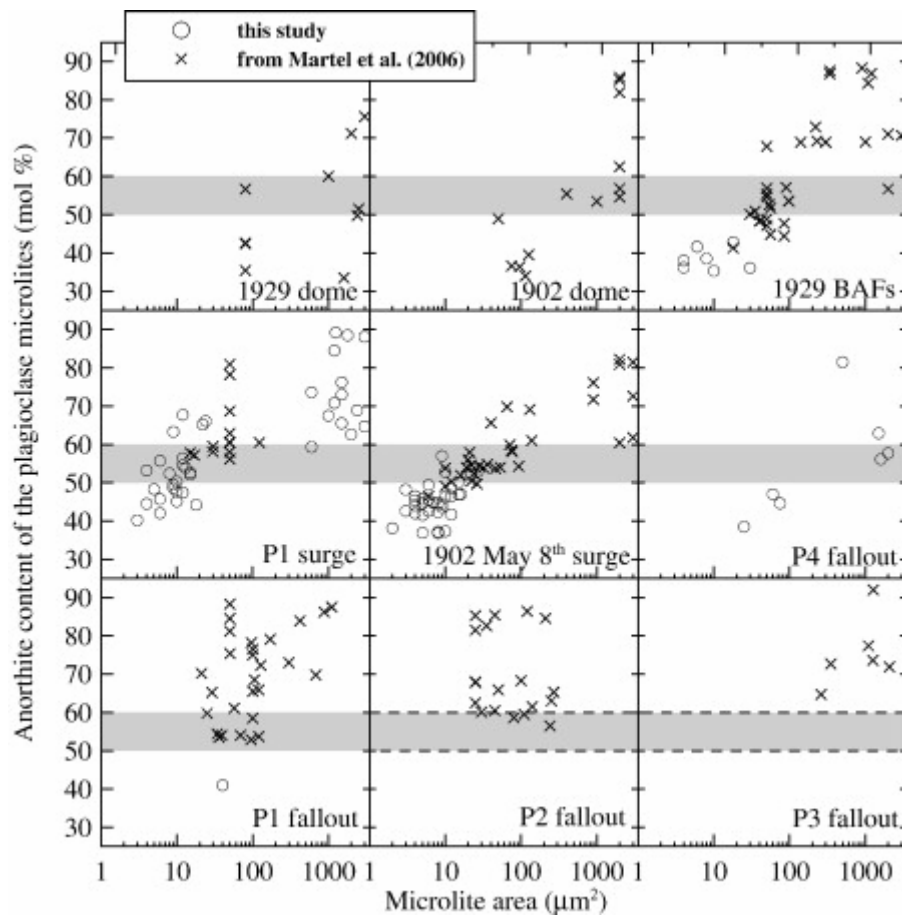


Fig. 3. Composition-size relation of the plagioclase microlites for different eruptive style deposits at Mt. Pelée. Chemically zoned microlites have been plotted with their core composition. The grey areas represent the  $An_{50-60}$  rim composition of the plagioclase phenocrysts (Martel et al., 1998), yet not statistically validated for the P2 and P3 eruptions (2 to 5 analyses of each deposit suggest similar or slightly more mafic ( $An_{55-65}$ ?) phenocryst rims).

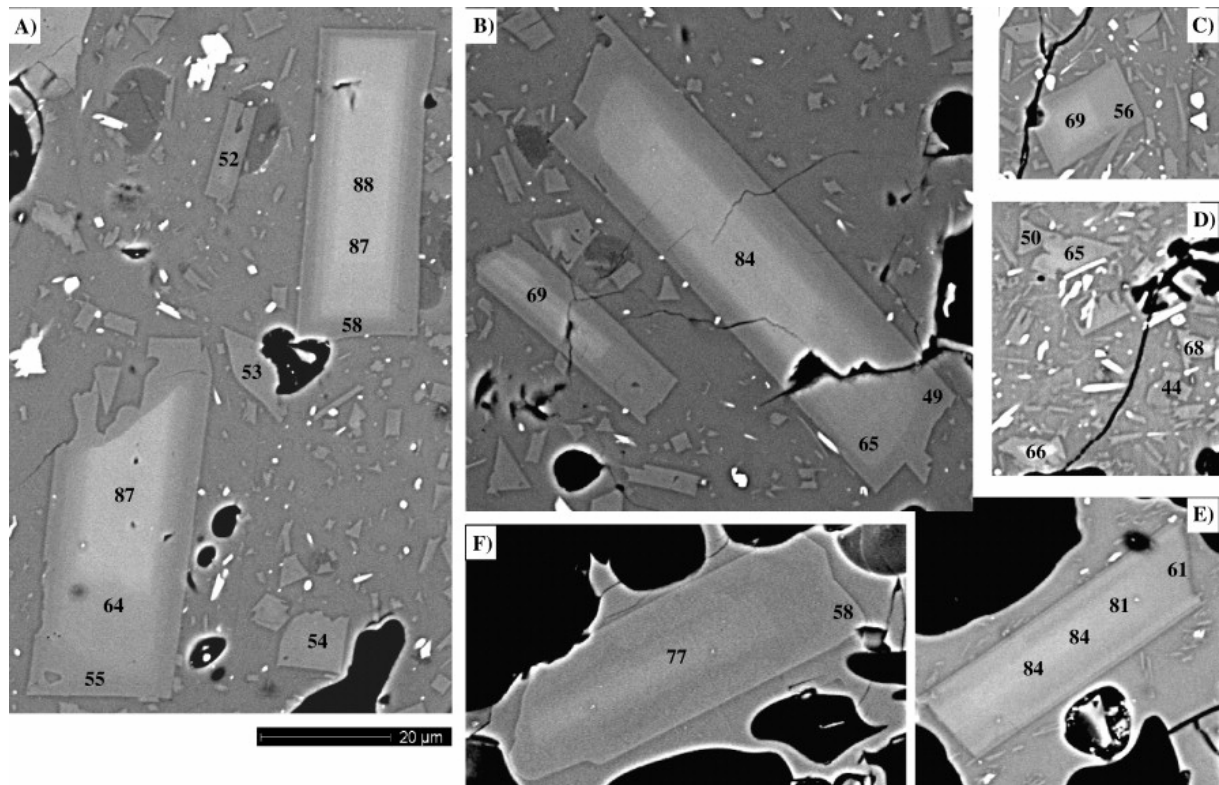


Fig. 4. SEM images of chemically-zoned plagioclase microlites. A–B) 1929 BAFs (MT37N1); C) 1902, May 8th surge (MT37B51); D) P1 surge (MT36P7); E) P1 plinian fallout (MT25E1); F) P3 plinian fallout (MT35G1). Scale bar of 20 µm for all images. Numbers are the analyzed anorthite molar content of the plagioclase (Martel et al., 2006).

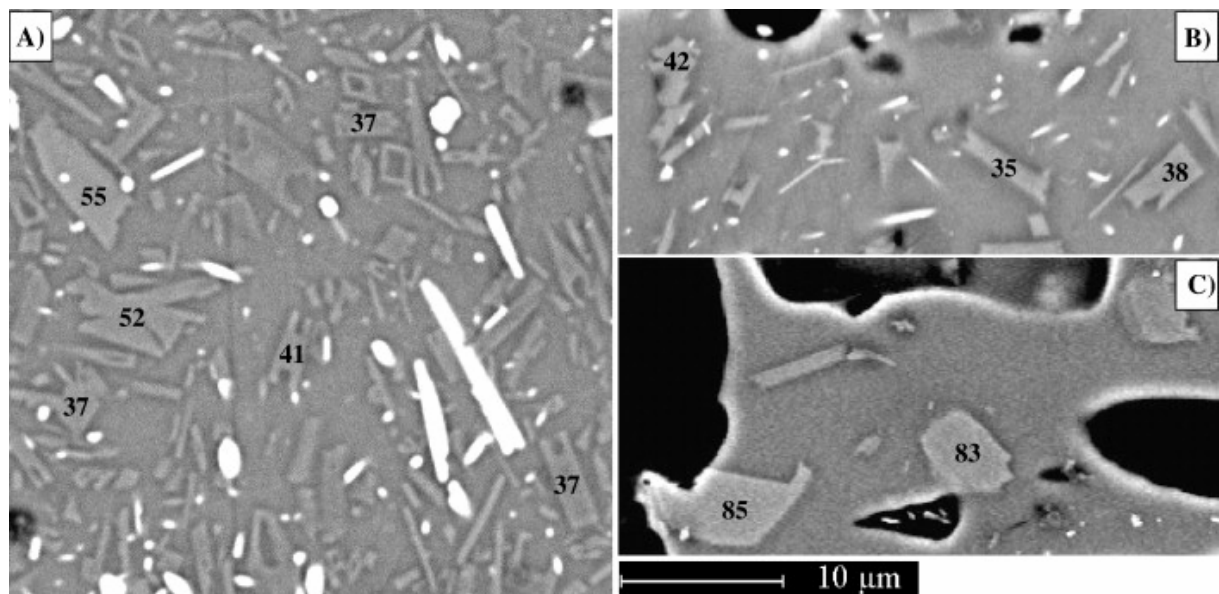


Fig. 5. SEM images of chemically-unzoned plagioclase microlites. A) 1902, May 8th surge (MT37B56); B) 1929 BAFs (MT37N1); and C) P2 fallout (MT37F). Numbers are the analyzed anorthite molar content of the plagioclase.

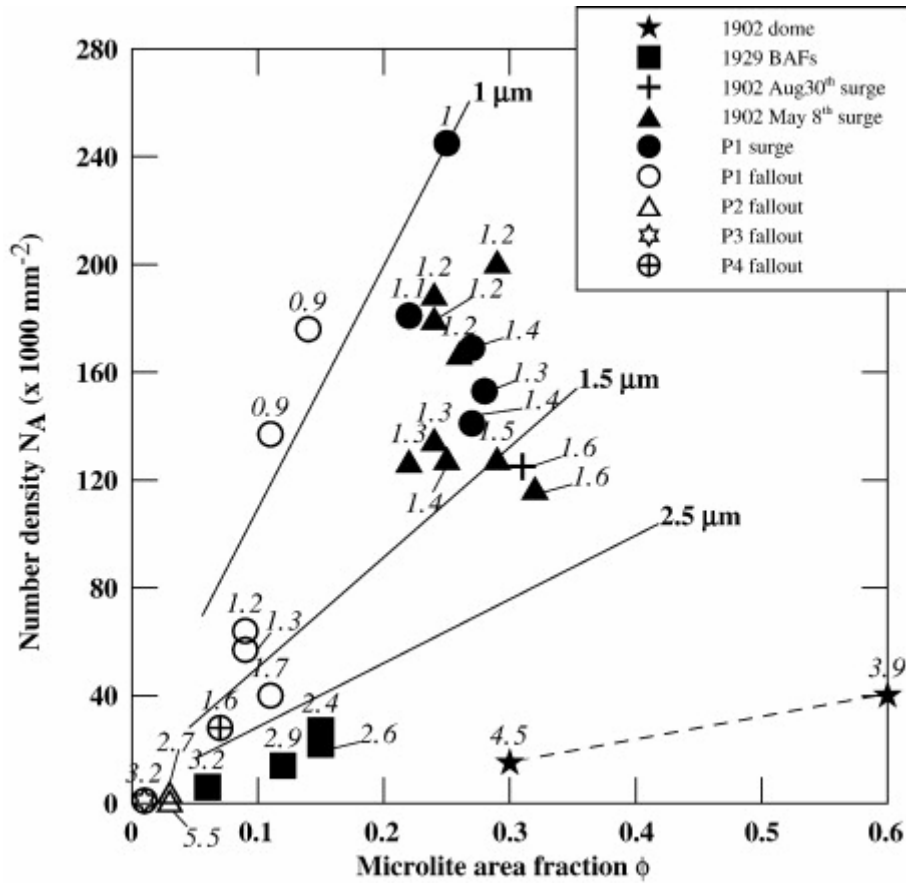


Fig. 6. Decompression-induced microlite  $\Phi$  versus  $N_A$  for different samples from recent eruptions of Mt. Pelée. The lines give the microlite mean size in  $\mu$ m ( $S_n$ ; Table 3). For samples of a given eruptive event, a vertical trend suggests a nucleation-dominated crystallization regime, and a horizontal trend suggests a growth-dominated crystallization regime (Hammer et al., 1999). The dashed line between the dome samples brackets  $\Phi$ , depending on whether the microlites are recalculated using the residual glass or the residual glass + silica precipitation (see text).

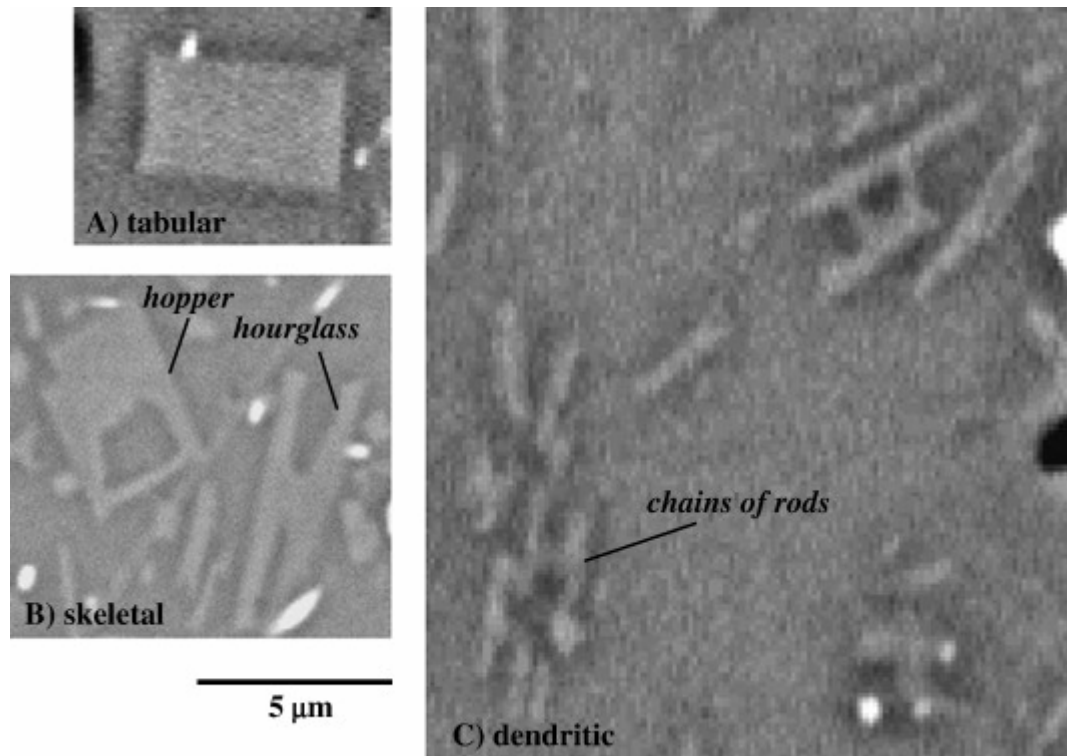


Fig. 7. SEM images of the plagioclase microlites morphologies. A) Tabular habit in a 1929 BAFs sample. The rectangular shape is observed in the [010] crystal orientation. For sections normal to [010], the crystal has an acicular or needle-like shape; B) Skeletal morphology in a 1902, May 8th surge sample, including hopper and hourglass shapes, depending on the axes along which the crystal is observed; C) Dendritic morphology characterized by chains of rods and swallowtails in a microlite-rich P1 plinian pumice.

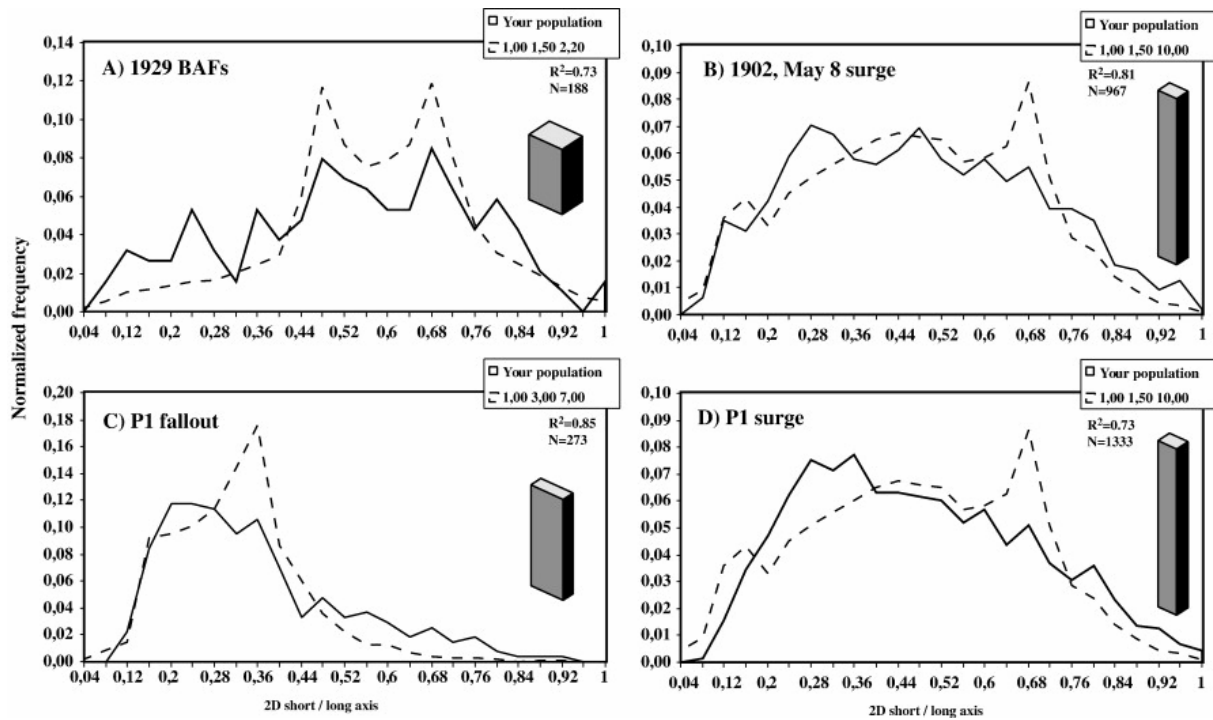


Fig. 8. Three-Dimensional habits of plagioclase microlites calculated after Morgan and Jerram (2006); A) 1929 BAFs (MT37N1); B) 1902, May 8th surge (MT37B19); C) P1 fallout (MT25E1); and D) P1 surge (MT36P6). The plain curves are the frequency histograms of the short to the long axis ratios measured in 2D for our data and the dashed lines represent the best-fit shape curve given for a 3D crystal habit (Long–Intermediate–Short axis).  $R^2$  gives the shape reliability and N is the number of counted microlites.

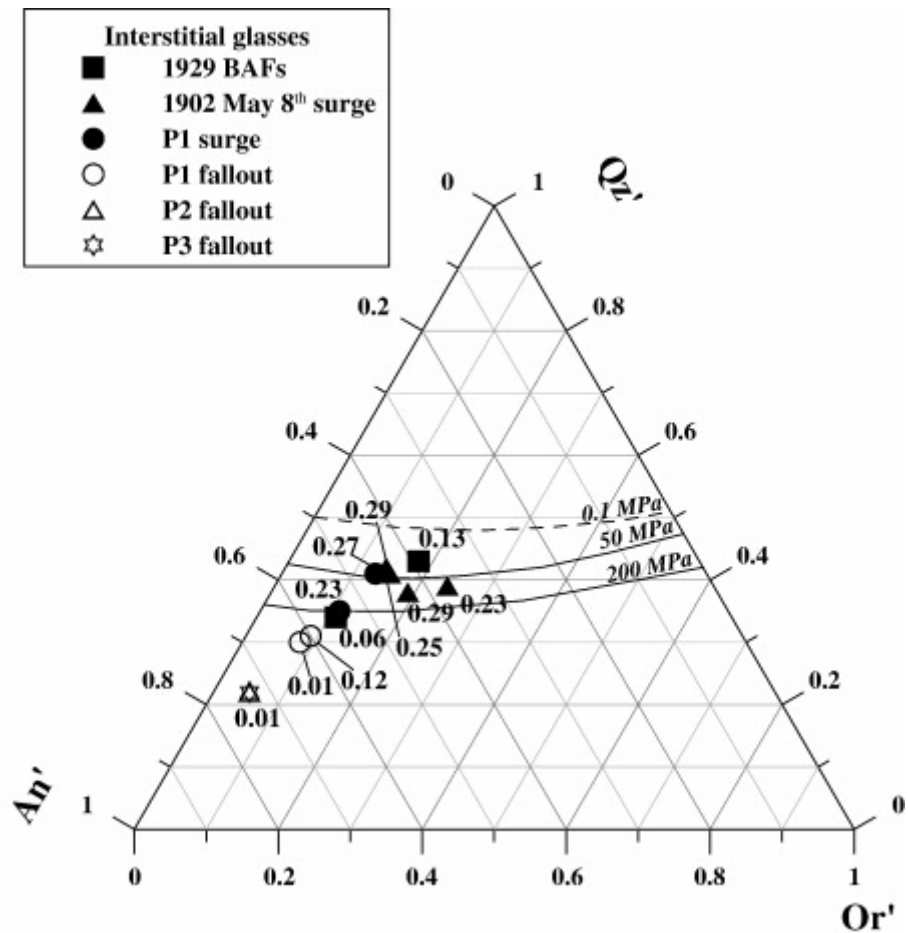


Fig. 9. Matrix glass compositions projected onto a Qz'-Ab'-Or' ternary, corrected for the presence of normative anorthite (< 15 wt.%); uncertainties up to 2 wt.%; after Blundy and Cashman (2001); The cotectic lines are drawn for a haplogranite melt Qz<sub>16</sub>Ab<sub>75</sub>Or<sub>9</sub> at 0.1 MPa (extrapolated), 50, and 200 MPa (Blundy and Cashman, 2001). Point labels give the area fraction of the decompression-induced plagioclase microlites.

**Tables**

Table 1. : Selected samples

Eruption unit	Eruption type	Lithology	Sample number
1929–32	Dome	Lithics	MT34P <sup>a,b</sup>
	Pelean BAFs	Lithics	MT37N1 <sup>ca</sup> , MT37N58 <sup>a</sup> , MT37N16 <sup>d</sup> , MT37N17 <sup>d</sup> , MT37N6 <sup>d</sup>
1902–04	Dome	Lithics	MT34M <sup>a</sup>
1902, May 8th	Pelean surge	Lithics	MT37B19 <sup>ca</sup> , MT37B56 <sup>ca</sup> , MT37B51 <sup>ca</sup> , MT37B82 <sup>d</sup> , MT37B6 <sup>d</sup> , MT37B55 <sup>d</sup>
1902, Aug 30th	Pelean surge	Lithics	MT36V15 <sup>ab</sup> , MT36V50 <sup>d</sup> , MT36V66 <sup>d</sup> , MT36V52 <sup>d</sup>
P1 (650 yr BP)	Plinian fallout	Pumice	MT25E1 <sup>ca</sup> , MT33C <sup>a</sup>
	Pelean surge	Lithics	MT36P6 <sup>ca</sup> , MT36P7 <sup>ca</sup>
P2 (1670 yr BP)	Plinian fallout	Pumice	MT37F <sup>ca</sup>
P3 (2010 yr BP)	Plinian fallout	Pumice	MT35G1 <sup>ca</sup>
P4 (2440 yr BP)	Plinian fallout	Pumice	MT32W <sup>ca</sup>

<sup>a</sup> Microlite fraction, size, and shape analyses.

<sup>b</sup> Porosity measurements determined by image analysis.

<sup>c</sup> Microlite compositional analyses.

<sup>d</sup> H<sub>2</sub>O content determined by ion probe.

Table 2. : Compositions and sizes of the plagioclase microlites

Eruption	Sample	No.	Size ( $\mu\text{m}^2$ )	Composition <sup>a</sup>									
				f	SiO <sub>2</sub>	FeO	Na <sub>2</sub> O	K <sub>2</sub> O	Al <sub>2</sub> O <sub>3</sub>	MgO	CaO	Total	An
1929	MT37N1	Q69	Glass	1.00	78.95	1.79	2.44	3.02	9.63	0.07	0.74	96.90	–
BAFs		Q72	30	0.25	60.32	0.47	7.26	0.18	23.88	0.01	7.53	99.57	36.06
		Q74	4	0.43	61.40	0.22	7.36	0.10	22.53	–0.05	7.62	99.08	36.19
		Q77	8	0.06	60.92	0.62	6.66	0.37	23.45	–	7.82	99.91	38.50
		Q78	10	0.56	60.49	0.58	7.15	0.02	23.65	0.19	7.08	99.32	35.32
		Q79	6	0.17	57.92	0.63	6.60	0.03	24.42	0.03	8.52	98.23	41.56
		Q70	Glass	1.00	78.07	1.42	2.68	2.76	10.91	0.10	1.12	97.43	–
		Q75	4	0.35	61.07	0.31	6.99	–0.08	24.09	0.06	7.77	100.19	38.05
1902	MT37B19	Q112	Glass	1.00	79.94	1.75	1.67	3.12	10.06	0.09	0.62	97.68	–
May 8th		Q84	6	0.15	58.32	0.68	6.05	0.17	25.29	0.01	9.69	100.18	46.50
surge		Q85	5	0.36	60.12	0.70	6.29	–0.03	24.39	0.05	9.16	100.68	44.59
		Q91	15	0.08	57.97	0.43	5.72	0.16	25.78	0.04	10.60	100.76	50.14
		Q92	2	0.35	61.73	0.39	7.09	0.01	22.71	–0.05	7.89	99.76	38.06
		Q94	4	0.25	60.07	0.34	6.67	0.06	24.25	–0.03	8.78	100.02	41.97
		Q104	5	0.20	58.94	0.63	6.25	0.08	24.78	0.03	9.61	100.37	45.73
		Q107	6	0.17	57.13	0.54	5.79	0.12	25.96	0.06	10.36	100.06	49.38
		Q110	4	0.24	59.00	0.39	6.16	0.12	25.33	0.05	9.83	101.02	46.54
		Q113	3	0.36	61.52	0.69	6.50	0.12	24.34	–0.02	8.82	101.93	42.56
		Q114	4	0.31	60.36	0.73	6.40	–	24.35	0.01	9.15	101.05	44.13
	MT37B56	Q132	Glass	1.00	79.52	1.88	2.13	2.61	10.03	0.07	0.90	97.61	–
		Q149	10	0.26	59.46	0.82	6.60	0.98	25.11	0.05	7.79	100.85	37.27
		Q153	8	0.30	60.41	0.70	6.45	1.38	23.51	0.04	7.76	100.34	36.82
		Q155	5	0.18	59.45	0.54	6.08	0.94	24.33	–0.02	8.59	99.89	41.47
		Q156	5	0.31	60.79	0.75	6.16	1.72	23.31	0.04	7.71	100.46	36.88
		Q157	16	0.18	57.68	0.75	5.76	0.58	25.72	0.03	9.86	100.46	47.01
		Q164	8	0.17	60.61	0.89	6.48	1.11	23.21	0.03	7.72	100.10	37.17
	MT37B51	Q115	9	0.10	54.94	0.32	4.86	0.12	27.97	0.07	11.85	100.16	57.00
		Q116	6	0.36	59.53	0.36	6.40	0.25	24.22	–	8.82	99.50	42.61
		Q117	9	0.32	58.59	0.61	6.07	0.49	24.24	0.03	8.96	99.03	43.65
		Q123	15	0.19	58.89	0.47	5.97	0.33	25.17	0.05	9.90	100.86	46.93
		Q124	10	0.06	57.15	0.87	5.23	0.14	26.28	–	10.78	100.51	52.81

Eruption	Sample	No.	Size ( $\mu\text{m}^2$ )	Composition <sup>a</sup>									
				f	SiO <sub>2</sub>	FeO	Na <sub>2</sub> O	K <sub>2</sub> O	Al <sub>2</sub> O <sub>3</sub>	MgO	CaO	Total	An
		Q126	8	0.23	58.53	0.61	6.22	0.26	25.37	–	9.30	100.23	44.57
		Q127	12	0.26	59.30	0.64	6.54	0.14	24.53	0.10	8.57	99.73	41.66
		Q128	7	0.32	59.16	0.48	6.25	0.21	24.76	0.07	9.34	100.21	44.69
		Q134	4	0.18	59.30	0.50	6.30	0.15	25.37	–0.02	9.62	101.29	45.38
		Q135	8	0.25	60.98	0.59	6.77	0.14	24.67	0.04	9.10	102.34	42.29
		Q136	9	0.23	59.89	0.42	6.21	0.34	23.96	0.04	9.33	100.17	44.49
		Q138	10	0.21	58.82	0.34	6.01	0.32	25.03	0.03	9.70	100.28	46.29
		Q139	6	0.19	58.35	0.31	6.23	0.10	25.16	0.02	9.54	99.79	45.57
		Q140	3	0.27	59.22	0.29	5.89	0.28	25.25	–0.03	10.23	101.16	48.20
		Q141	12	0.20	57.24	0.71	5.76	0.16	25.31	0.14	9.98	99.31	48.46
		Q143	12	0.21	60.26	0.60	6.32	0.10	25.62	0.01	10.05	102.90	46.51
P1 fallout	MT25E1	T3	Glass	1.00	75.42	2.73	1.48	2.07	12.93	0.33	2.06	97.26	–
		T9	40	0.14	58.90	0.40	6.75	–	25.21	0.03	8.50	99.87	41.03
P1 surge	MT36P7	Q4	9	0.00	54.51	0.59	3.93	0.26	27.82	–	12.79	100.05	63.27
		Q14	22	0.00	52.29	0.30	3.97	0.14	28.89	0.04	13.75	99.48	65.18
		Q15	10	0.00	57.84	0.68	5.53	0.28	25.79	–	10.48	100.71	50.31
		Q11	Glass	1.00	75.57	2.61	2.29	1.97	11.26	0.28	2.16	96.59	–
		Q3	3	0.61	59.47	0.59	6.88	0.14	25.34	0.22	8.50	101.16	40.25
		Q5	8	0.07	56.66	0.68	5.40	0.13	26.97	–	10.92	100.77	52.38
		Q30	Glass	1.00	77.57	2.34	1.76	2.23	10.81	0.18	1.95	97.22	–
		Q17	12	0.15	53.92	0.31	4.69	0.15	25.62	0.04	11.20	96.01	56.38
		Q18	4	0.14	57.45	0.63	5.17	0.01	26.01	0.05	10.65	100.04	53.20
		Q19	9	0.29	57.74	0.57	5.70	0.11	25.66	–0.07	10.25	100.04	49.53
		Q20	10	0.42	57.22	0.64	5.97	0.19	24.01	–0.10	9.08	97.18	45.15
		Q21	18	0.34	56.33	0.98	6.18	0.27	25.33	0.17	9.12	98.44	44.22
		T43	1200	0.00	50.79	0.38	3.33	0.06	31.28	0.02	14.79	100.71	70.80
		T44	3000	0.00	46.09	0.60	1.33	0.06	34.00	0.07	18.35	100.51	88.15
		T45	1200	0.00	46.62	0.63	1.78	0.05	33.96	0.09	17.82	100.99	84.48
		T47	1000	0.00	51.73	0.66	3.76	0.06	30.36	0.08	14.25	101.10	67.47
	MT36P6	Q37	Glass	1.00	79.07	2.28	2.03	2.33	10.32	0.21	1.35	97.97	–
		Q34	13	0.07	55.99	0.46	5.23	0.07	27.23	–0.02	11.18	100.11	53.94
		Q40	9	0.14	58.31	0.36	5.68	0.31	25.27	0.05	10.05	100.02	48.56
		Q41	6	0.34	59.58	0.44	6.12	0.24	25.12	–	9.56	100.96	45.70

Eruption	Sample	No.	Size ( $\mu\text{m}^2$ )	Composition <sup>a</sup>									
				f	SiO <sub>2</sub>	FeO	Na <sub>2</sub> O	K <sub>2</sub> O	Al <sub>2</sub> O <sub>3</sub>	MgO	CaO	Total	An
		Q42	4	0.38	59.05	0.72	6.34	0.12	24.67	-0.10	9.33	100.23	44.54
		Q43	12	0.17	58.96	0.64	5.97	0.17	24.96	-0.04	9.93	100.61	47.43
		Q46	6	0.36	60.77	0.18	6.65	0.29	24.80	-0.10	8.98	101.56	42.04
		Q57	Glass	1.00	77.16	1.85	2.47	2.07	11.96	0.08	2.07	98.15	-
		Q47	15	0.24	55.63	0.71	5.27	0.16	26.80	-0.02	10.80	99.39	52.61
		Q48	6	0.33	56.42	0.37	5.10	0.09	29.96	0.01	11.72	103.69	55.66
		Q51	10	0.23	57.52	0.49	5.88	0.14	25.82	-0.02	9.84	99.74	47.66
		Q55	5	0.42	58.57	0.54	5.99	0.04	25.95	0.05	10.18	101.26	48.32
		Q58	12	0.06	56.38	0.40	4.96	0.30	26.51	-	11.24	99.85	54.63
		T33	1250	0.00	46.40	0.47	1.19	0.05	34.15	-	18.35	100.61	89.23
		T34	2400	0.00	51.31	0.61	3.58	0.05	30.86	0.08	14.48	101.04	68.90
		T35	600	0.00	49.86	0.56	2.92	0.08	31.22	0.11	15.01	99.87	73.58
		T36	3000	0.00	52.36	0.45	3.94	0.06	30.06	0.02	13.17	100.07	64.67
		T37	1500	0.00	49.68	0.53	2.68	-	32.89	0.06	15.56	101.40	76.25
		T38	1500	0.00	50.50	0.78	3.01	0.04	31.53	0.08	14.90	100.84	73.05
		T39	2000	0.00	53.13	0.62	4.26	0.09	29.63	0.06	13.10	100.91	62.62
		T40	600	0.00	53.42	0.46	4.57	0.09	28.81	0.02	12.21	99.75	59.31
		T41	1500	0.00	51.85	0.71	3.96	-	29.66	0.06	13.62	99.88	65.55
		T42	1800	0.00	45.53	0.61	1.29	0.04	34.37	-	18.31	100.15	88.49
P4 fallout	MT32W	T54c	500	0.00	47.92	0.51	2.02	-	32.66	0.01	16.04	99.24	81.46
		T55r	500	0.00	54.68	0.36	4.67	0.16	28.24	-	11.90	100.02	57.92
		T57	2000	0.00	54.28	0.47	4.71	0.13	29.09	0.02	11.82	100.52	57.66
		T60	1500	0.00	52.57	0.38	4.12	0.11	30.04	0.06	12.86	100.22	62.86
		T61	1600	0.00	55.07	0.31	4.81	0.12	28.53	-	11.32	100.37	56.14
		T63	Glass	1.00	74.39	1.63	2.36	1.74	12.42	0.22	2.40	95.43	-
		T50	60	0.11	58.27	0.39	6.02	0.01	26.67	0.01	9.68	101.14	47.02
		T51	75	0.07	58.33	0.34	6.21	0.14	26.16	-	9.18	100.40	44.60
		T52	25	0.47	57.51	0.29	6.76	0.21	24.68	0.07	7.80	97.49	38.46

<sup>a</sup> Chemical composition in wt.% (MnO and TiO<sub>2</sub> < 0.2 wt.%; see text for the recalculation procedure); An for anorthite content in mol.%; All Fe as FeO; *f* for the calculated mixing fraction between the glass (composition referred as "Glass") and the following plagioclases.

Table 3. : Fractions and textural characteristics of the plagioclase microlites

Deposit	Sample	Porosity fraction	$n^a$	2-Dimensions <sup>b</sup>				3-Dimensions <sup>c</sup>		
				$\Phi$	$N_A \times 10^3$ (mm <sup>-2</sup> )	$S_n$ ( $\mu\text{m}$ )	Shape	S:I:L axis	$R^2$	Shape
1929 dome	MT34P	0.15	~ 100	0.30–0.60 <sup>d</sup>	15–40 <sup>d</sup>	4.5–3.9 <sup>d</sup>	T	n.d.	n.d.	n.d.
1929 BAF	MT37N1	0.44	105	0.15	22	2.6	T+S	1.0:1.5:2.2	0.73	acicular
			83	0.12	14	2.9	T + S			
			2	0.07	< 1		T + S	n.d.	n.d.	n.d.
	MT37N89	0.35	7	0.10	< 1		T	n.d.	n.d.	n.d.
	MT37N58	0.15	64	0.15	27	2.4	S + T	1.0:1.5:1.8	0.59	rectangular prism
	MT36A	n.d.	31	0.06	6	3.2	S + T	n.d.	n.d.	n.d.
1902 dome	MT34M	0.15	~ 100	0.30–0.60 <sup>d</sup>	15–40 <sup>d</sup>	4.5–3.9 <sup>d</sup>	T	n.d.	n.d.	n.d.
1902, Aug 30th surge	MT36V15	0.31	110	0.31	125	1.6	S + T	1.0:1.6:8.0	0.67	acicular
			10	0.18	< 1		T	n.d.	n.d.	n.d.
	MT36V4	0.32	25	0.21	< 1	n.d.	T	n.d.	n.d.	n.d.
1902, May 8th surge	MT37B56	0.26	237	0.24	135	1.3	S	1.0:2.7:8.0	0.72	acicular
			295	0.22	127	1.3	S			
	MT37B51	0.39	281	0.25	128	1.4	S	1.0:1.5:10.0	0.75	acicular
			443	0.32	117	1.6	S			
			279	0.29	128	1.5	S			
	MT37B19	0.37	338	0.24	180	1.2	S	1.0:1.5:10.0	0.81	acicular
			255	0.26	167	1.2	S			
			374	0.24	189	1.2	S			
	MT37B23	0.35	100	0.29	201	1.2	S	n.d.	n.d.	n.d.
			8	0.05	< 1		T	n.d.	n.d.	n.d.
P1 surge	MT36P6	0.29	443	0.27	141	1.4	S+D	1.0:1.5:10.0	0.73	acicular
			466	0.27	169	1.4	S + D			
			424	0.28	153	1.3	S + D			
	MT36P7	0.68	319	0.25	245	1.0	S + D	1.0:2.1:6.0	0.71	acicular

Deposit	Sample	Porosity fraction	$n^a$	2-Dimensions <sup>b</sup>				3-Dimensions <sup>c</sup>		
				$\Phi$	$N_A \times 10^3$ (mm <sup>-2</sup> )	$S_n$ ( $\mu\text{m}$ )	Shape	S:I:L axis	$R^2$	Shape
			221	0.22	181	1.1	S + D			
P1 fallout	MT25E1	0.57	32	0.11	137	0.9	D	1.0:3.0:7.0	0.85	rectangular prism
			74	0.14	176	0.9	D			
			54	0.11	40	1.7	D			
			69	0.09	57	1.3	D			
			76	0.09	64	1.2	D			
	MT33C	0.61	4	<i>0.01</i>	<i>&lt; 1</i>	3.2	<i>T</i>	<i>n.d.</i>	<i>n.d.</i>	<i>n.d.</i>
			2	<i>0.01</i>	<i>&lt; 1</i>	3.2	<i>T</i>	<i>n.d.</i>	<i>n.d.</i>	<i>n.d.</i>
P2 fallout	MT37F	0.72	7	<i>0.03</i>	<i>1</i>	5.5	<i>T</i>	<i>n.d.</i>	<i>n.d.</i>	<i>n.d.</i>
			36	<i>0.03</i>	<i>4</i>	2.7	<i>T</i>	<i>1.0:2.5:4.0</i>	<i>0.64</i>	<i>rectangular prism</i>
P3 fallout	MT35G1	0.66	1	<i>0.01</i>	<i>&lt; 1</i>	3.2	<i>T</i>	<i>n.d.</i>	<i>n.d.</i>	<i>n.d.</i>
P4 fallout	MT32W	0.79	44	0.07	28	1.6	S	1.0:6.0:10.0	0.73	rectangular prism

n.d. = not determined. Values in italic refer to the basalt-inherited microlites, whereas the other are decompression-induced microlites (see Discussion).

<sup>a</sup> Number of analyzed microlites.

<sup>b</sup>  $\Phi$  = area fraction;  $N_A$  = number density;  $S_n$  = mean size, equals to  $10^3 \times (\Phi/N_A)^{0.5}$ ; *T* for tabular, *S* for skeletal, and *D* for dendritic.

<sup>c</sup> 3-D recalculation after Morgan and Jerram (2006). S:I:L for Short, Intermediate, and Long axis, respectively;  $R^2$ : fractional measure of the variation.

<sup>d</sup> The first value is calculated on a groundmass including the silica phase; the second value is for a silica-free groundmass melt (see text for explanation).

Table 4. : Glass compositions of Mt. Pelée

Eruption	Sample	<i>n</i>	SiO <sub>2</sub>	FeO	Na <sub>2</sub> O	K <sub>2</sub> O	Al <sub>2</sub> O <sub>3</sub>	MgO	CaO	Qz',Ab',Or'
1929 BAFs	MT37N1	6	79.44(58)	1.54(32)	4.40(18)	2.92(11)	10.31(41)	0.05(04)	0.88(18)	43,39,18
	MT36A	10	76.92(80)	2.02(26)	4.43(21)	2.31(10)	12.03(40)	0.25(05)	1.65(18)	34,55,11
1902 May 8th	MT37B56	10	77.79(67)	2.04(41)	3.79(51)	3.96(23)	10.80(32)	0.07(04)	1.03(21)	39,37,24
	surge	MT37B51	10	80.06(77)	1.74(20)	3.76(31)	2.62(11)	10.26(54)	0.08(04)	1.07(28)
	MT37B19	6	79.56(75)	1.91(10)	3.60(40)	3.03(15)	10.50(21)	0.05(03)	0.89(21)	41,44,15
	MT37B23	2	78.19(73)	1.79(04)	3.08(22)	3.69(02)	11.42(53)	0.16(03)	1.27(03)	38,43,19
P1 surge	MT36P7	7	77.93(79)	2.55(16)	3.19(43)	2.24(15)	11.50(43)	0.18(05)	1.97(28)	35,54,11
	MT36P6	4	79.80(12)	2.19(32)	3.45(28)	2.44(07)	10.34(29)	0.15(12)	1.18(19)	41,46,13
P1 fallout	MT25E1	3	76.37(15)	2.59(09)	3.34(14)	2.10(02)	12.59(06)	0.41(05)	2.23(10)	31,60,9
	MT33C	5	76.72(17)	2.20(10)	3.62(15)	1.93(04)	12.60(13)	0.32(04)	2.21(01)	30,62,8
P2 fallout	MT37F	10	73.36(68)	2.94(14)	4.27(24)	1.80(12)	14.02(20)	0.54(05)	2.83(14)	22,73,5
P3 fallout	MT35G1	5	72.94(22)	2.92(23)	4.27(24)	1.70(08)	14.15(21)	0.59(03)	3.08(09)	22,73,5

Compositions recalculated to 100 wt.%; *n* is the number of analyzes; numbers in brackets are the statistical errors on the two last digits; Qz',Ab',Or' is the normative quartz (Qz'), albite (Ab'), and orthose (Or') composition obtained from the CIPW norms of the glasses and corrected to account for the displacement of the quartz–feldspar cotectic in presence of normative anorthite (< 20 wt.%; corindon < 1 wt.%), as explained in Blundy and Cashman (2001).

Table 5. : H<sub>2</sub>O contents of the interstitial glasses

Eruption	Sample	Porosity fraction	<i>n</i>	H <sub>2</sub> O content (wt.%) <sup>a</sup>			Pressure <sup>b</sup> (MPa)	Depth <sup>c</sup> (m)
				Mean (± σ)	Max	Min		
1929 BAFs	MT37N16	0.12	2	0.17 (0.01)	0.17	0.16	0.1	4
	MT37N17	0.30	2	0.67 (0.32)	1.12	0.22	5.1 (3.9–5.8)	231
	MT37N6	0.40	2	0.93 (0.05)	1.03	0.84	9.7 (8.7–10.7)	434
1902 May 8th	MT37B82	0.17	7	0.36 (0.05)	0.50	0.21	1.2 (0.9–1.7)	58
surge	MT37B6	0.30	2	0.40 (0.06)	0.48	0.32	1.6 (1.1–2.2)	71
	MT37B55	0.44	5	0.68 (0.05)	0.81	0.59	5.3 (4.5–6.1)	240
1902 Aug 30th	MT36V50	0.13	3	0.41 (0.05)	0.50	0.30	1.7 (1.2–2.2)	80
surge	MT36V66	0.35	5	0.61 (0.23)	1.14	0.13	4.2 (1.4–8.0)	191
	MT36V52	0.51	2	0.84 (0.33)	1.31	0.38	8.0 (2.8–14.8)	359
P1 fallout <sup>d</sup>	MT33C	0.61	4	1.8 (0.3)	2.3	1.6	31.7 (23.1–41.1)	1414
P2 fallout	MT37F	0.72	10	2.47 (0.33)	3.14	1.34	53.9 (42.4–66.3)	2390

*n* is the number of analyzed glasses.

<sup>a</sup> Determined by ion probe (see text for analytical procedure), except for the P1 and P2 fallout samples, for which glass H<sub>2</sub>O were determined by the “by-difference” method using the electron microprobe.

<sup>b</sup> H<sub>2</sub>O saturation pressures deduced from the empirical equation of H<sub>2</sub>O solubility at 875 °C (see text) for the mean H<sub>2</sub>O content (± σ).

<sup>c</sup> Calculated from saturation pressures with an average rock density of 2.3 g/cm<sup>3</sup>.

<sup>d</sup> Data from Martel et al. (2000).